Future climate-induced changes in mixing and deep oxygen content of a caldera lake with hydrothermal heat and salt inputs

Tamara Wood [a], Susan Wherry [a], Sebastiano Piccolroaz [b], Scott Girdner [c,*]

[a] US Geological Survey Oregon Water Science Center, 2130 SW 5th Ave., Portland, OR 97201, USA
[b] Department of Civil, Environmental, and Mechanical Engineering, University of Trento, via Mesiano 77, I-38123 Trento, Italy
[c] Crater Lake National Park, 1 Sager Building, Crater Lake, OR 97604, USA

ARTICLE INFO

ABSTRACT

Vertical profiles of temperature, salinity and dissolved oxygen in Crater Lake, a caldera lake in the Oregon Cascade Range that receives hydrothermal inputs of heat and salt, were simulated with a 1-dimensional model. Twelve Global Circulation Models and two Representative Concentration Pathways (RCPs) were used to develop boundary conditions from 1950 to 2099. The model simulated the ventilation of deep water initiated by reverse stratification and subsequent thermobaric instability. All models predicted a reduction in the frequency of deep ventilation events, from an ensemble median frequency of 5.4 winters decade^{-1} during 1950–2005 to 4.3 (RCP4.5) or 2.5 (RCP8.5) winters decade^{-1} during 2045–2099. Favorable conditions for thermobaric instability-induced mixing currently occur infrequently and will become rare in the future. The salinity gradient resulting from hydrothermal inputs presents an additional barrier to thermobaric instability that will continue through 2099. A redistribution of salt to the deep lake may prevent ventilation all the way to the bottom in the future. Hypolimnetic dissolved oxygen percent saturation remained above 75% within the 21st century, consistent with oligotrophy and very small oxygen demands. The rate of change in all variables accelerated approaching 2099, coincident with elimination of winter reverse stratification. Historically, about half of the hydrothermal heat added to Crater Lake has been vented to the atmosphere. In the RCP8.5 scenario, the hydrothermal heat will cease to be vented to the atmosphere by the end of the 21st century, and then the temperature of the deep waters will increase rapidly.

Introduction

Vertical mixing processes in lakes directly control the internal distribution of heat, recycling of nutrients, and replenishment of dissolved oxygen at the lake floor (Boehrer et al., 2008; Carmack and Vagle, 2021; van Haren et al., 2020). Most lakes routinely mix to the bottom convectively, but some very deep lakes require the occurrence of thermobaric instability to exchange water between the surface and bottom. In one dimension and with no salinity gradient (Boehrer et al., 2008) thermobaric instability arises when an inversely stratified temperature profile moves vertically across the profile of the temperature of maximum density as a result of wind-induced seiching, internal waves, or downwelling at a shoreline. In three dimensions the mechanism can be described as a tilting of the base of the thermocline such that

colder surface water is displaced downward to a depth where it has the same density as warmer water at the same depth but on the other side of the thermocline (Carmack and Weiss, 1991). In either case there will be no positive buoyancy force on the colder water and it will continue to sink to the bottom or to the depth where it once again encounters water of the same density, a process called deep ventilation. Examples of such lakes include the deepest lake in the world (Lake Baikal), the three deepest lakes in North America (Great Slave Lake, Crater Lake, and Quesnel Lake), numerous deep fjord lakes in Norway, and crater lakes in Japan (Shikotsu Lake).

Because deep ventilation involves the exchange of cold surface water (<4 °C) with warmer water at the bottom, the hypolimnetic temperature of a lake is reset when deep ventilation occurs between the temperature of maximum density (T_{md}) at the surface (∼3.98 °C) and the T_{md} at the bottom (T_{md} declines 0.021 °C per 100 m). The response of the hypolimnetic temperature to a warming climate on decadal scales is therefore determined by the frequency of deep ventilation. Modeling studies have shown that

---

* Corresponding author.

E-mail addresses: tmwood@usgs.gov (T. Wood), Scott_Girdner@nps.gov (S. Girdner).

deep ventilation initiated by thermobaric instability, which requires reverse stratification and adequate wind energy input at the surface, may happen less frequently as the climate warms (Piccolroaz and Toffolon, 2018; Wood et al., 2016).

Crater Lake, Oregon (USA) is a deep caldera lake located at 1883 m elevation near the crest of the Cascade Range within Crater Lake National Park. Periods of convective mixing in early winter and spring are limited to depths of 300–400 m, but less frequent deep ventilation initiated by thermobaric instability is the primary mechanism by which Crater Lake mixes to the 594 m bottom (Crawford and Collier, 2007). The less frequent deep ventilation events reset profundal temperature, as well as replenish dissolved oxygen, and reduce nutrients and salinity in the deep water. Crater Lake is situated at an intersection of altitude and latitude that makes it particularly susceptible to warming trends in air temperature. Under current conditions, the lake rarely freezes over, and wintertime reverse stratification (a necessary condition for thermobaric instability) does not occur every year. Furthermore, Crater Lake receives hydrothermal inputs to the floor of the lake that provide a flux of heat and salinity to the hypolimnion.

Thermobaricity was not initially understood to be the mechanism for deep ventilation of Crater Lake. Early microstructure measurements revealed a persistently hyperadiabatic temperature gradient below 300 m depth (Neal et al., 1972) that necessitated a compensating salinity gradient to produce a stable density structure (McManus et al., 1993; Collier et al., 1990). This contrasts with other very deep lakes such as Great Bear Lake (Johnson, 1966; maximum depth 450 m), Quesnel Lake (Laval et al., 2012; maximum depth 511 m) and Great Slave Lake (Carmack and Vagle, 2021, maximum depth 614 m), in which the winter and early spring temperature gradient below a mid-depth maximum (the thermobaric horizon, Carmack and Vagle, 2021) is between the slope of the temperature of maximum density and the slope of maximum stability (1/2 the gradient of the temperature of maximum density; Eklund, 1965). Crawford and Collier (1997) noted that the conditions did not seem favorable for thermobaric instabilities to set up in Crater Lake because the density difference between colder water displaced downward from the surface and warmer water at depth would have to overcome the stable salinity gradient. With more measurements, it became clear that thermobaric instabilities were responsible for ventilation of the deepest layers (Crawford and Collier, 2007). Further, Wood et al. (2016) showed that the state-of-the-art one-dimensional lake model DYRESM (Imerito, 2014) that has been used to accurately simulate convective mixing processes in moderately deep lakes (for example Lake Geneva; Perroud et al., 2009), but does not allow the possibility of modelling thermobaricity, could not simulate deep ventilation in Crater Lake.

Deep ventilation initiated by thermobaric instabilities is inherently a 3-dimensional phenomenon that can be enhanced by a long, narrow geometry through the development of coastal downwelling in the presence of persistent along-lake winds (Boehrer et al., 2013; Carmack and Weiss, 1991). Deep ventilation is observed to be a 3-dimensional phenomenon in Crater Lake even though it is relatively small and nearly circular with a diameter of about 8 km (Crawford and Collier, 2007). Internal Poincaré or Kelvin waves are a likely response to wind disturbance in winter and could produce the necessary tilting of the thermocline to initiate thermobaric instability (Crawford and Collier, 2007). This presents a challenge for modeling the response to climate over several decades, as detailed 3-dimensional hydrodynamic models that could resolve internal waves would be computationally prohibitive.

In a previous study, the 1-Dimensional Deep Ventilation (1DDV) model first developed to simulate deep ventilation in Lake Baikal (Piccolroaz and Toffolon, 2013) was used to investigate the response of mixing in Crater Lake to climate change. In that study, salinity was not simulated dynamically; rather, the salinity profile was held fixed at a historical average, thus maintaining a consistent stabilizing effect of salinity through time (Wood et al., 2016). In reality, the salinity gradient evolves gradually between mixing events, and is reset abruptly when surface and bottom water are exchanged during deep ventilation. The salinity gradient can be expected to vary between larger extremes as the length of time between deep ventilation events increases in the future, and for this reason, the effect of a dynamically varying salinity on the frequency of deep ventilation is uncertain.

In this study we used a modification of 1DDV that dynamically simulated salinity as well as temperature. We determined how the inclusion of dynamic salinity modifies the projections of the change in mixing frequency in response to a warming climate. We then used the model to simulate the profundal changes in dissolved oxygen concentration resulting from the change in mixing frequency. We used an ensemble of 12 general circulation models to generate lake surface boundary conditions, building on the work of Wood et al. (2016) in which deep ventilation in Crater Lake was simulated with three GCMs and with a coarser lake model resolution.

Methods

Historical water quality and meteorological data

High frequency meteorological and water quality data have been collected at Crater Lake since 1990, and lake surface elevation has been measured sporadically since 1901, with consistent sub-daily measurements beginning in 1961 (Crawford and Collier, 2007; Redmond, 2007). Meteorological data include wind speed, air temperature, relative humidity, shortwave solar radiation, and daily accumulation of rain and snow precipitation. Wind speed, air temperature, and relative humidity were collected year-round at 1-hour intervals from a buoy in the North Basin of the lake at site B (Fig. 1) at a height of 2 m above water surface. Small gaps in the buoy data were filled using data from a meteorological station located on the crater rim, where solar radiation is also measured (Wood et al., 2016). Daily accumulation of rain and snow were collected at Crater Lake National Park Headquarters (National Weather Service cooperative station ID 35-1946), located 1.5 km from the crater rim on the south side of Mount Mazama (Fig. 1). Long-term meteorological data from the crater rim have been used to estimate seepage rates from the lake (Redmond, 1990) and to develop monthly average rates of lake-surface precipitation and evaporation (Redmond, 2007).

The water quality datasets used to calibrate the model included hourly surface water temperature collected at the floating weather buoy located at site B, as well as water temperature collected by internally recording thermistors (10-minute intervals) at 17 discrete depths ranging from 20 to 580 m on a rope mooring at site B. Temperature data were collected with two types of thermistors, Alpha-Omega MDR 9102 and SeaBird Scientific SBE 39. Thermistors were calibrated every 2–4 years with uncertainties estimated at +/- 0.002 °C (Crawford and Collier, 2007). Based on the overlapping availability of water temperature and wind speed data (required to prescribe the boundary conditions of the 1-Dimensional Deep Ventilation model described in the following sections), the 22-year period between July 10, 1992 and July 8, 2013 was used for model calibration and validation.

In addition to the high-frequency thermistor data at 18 depths, water column profiles of temperature and salinity were collected with a SeaBird Scientific model SBE19 conductivity, temperature, and depth profiling sensor (CTD), deployed from a research vessel
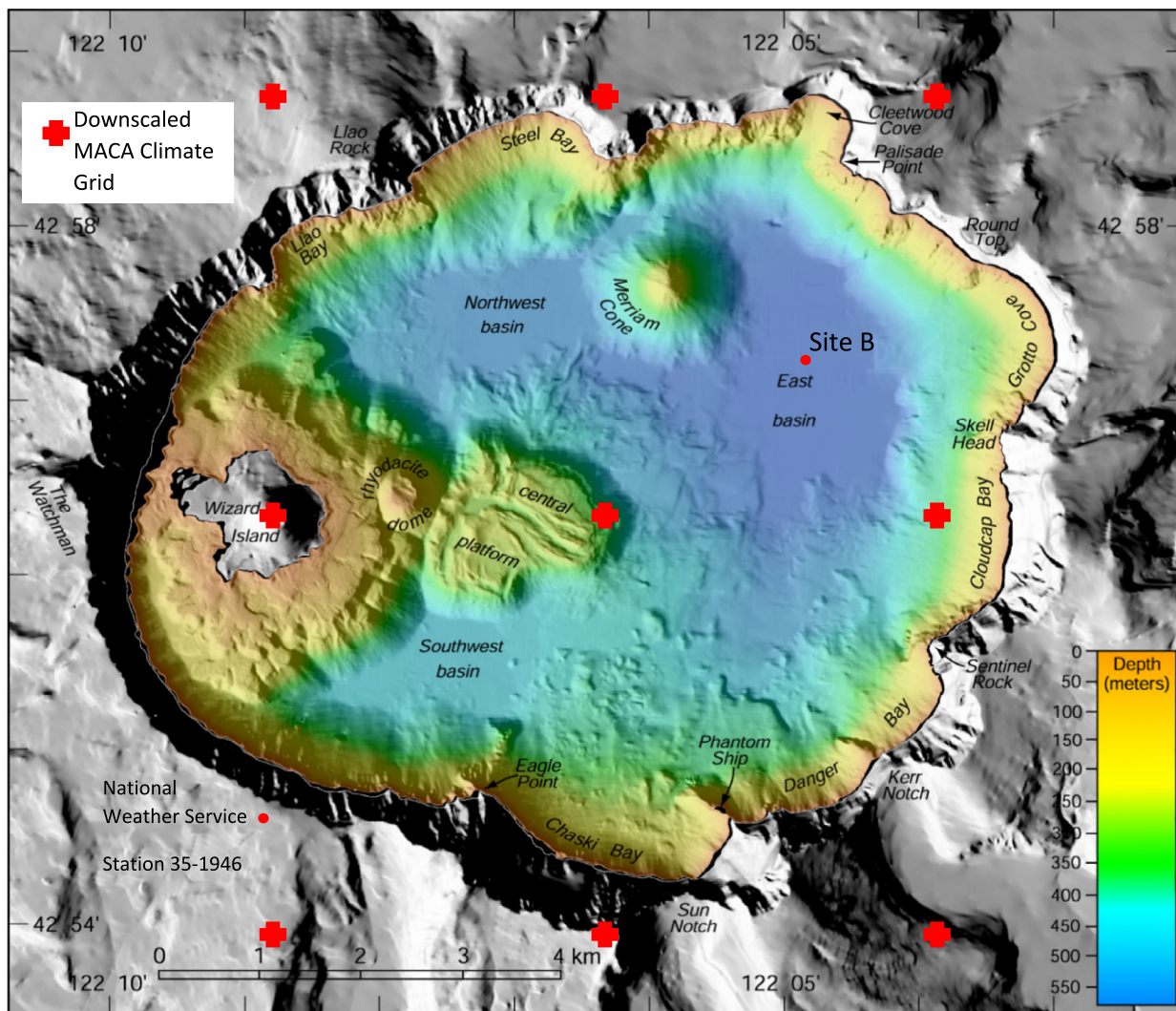
Fig. 1. Map of Crater Lake, Oregon.

during discrete sampling events primarily between June and October 1988 to 2013 at site B. Absolute accuracy of the temperature sensor is estimated to be about 0.005 °C (Crawford and Collier, 2007). Salinity was determined from conductivity using a relationship developed for Crater Lake (McManus et al., 1992). Data were collected at 2 Hz and binned to 1-m depth intervals. The data from these profiles were used to evaluate: 1) initial conditions in the lake to be used in the modeling; 2) temperature- and salinity-specific turbulent diffusivity profiles of the water column; and 3) rates of deep-lake heat and salinity fluxes due to hydrothermal inputs.

Long-term primary productivity data using the Carbon-14 light/dark bottle method were used to estimate mean phytoplankton oxygen production within the water column. Primary productivity was determined monthly during summer by the Crater Lake Long-Term Monitoring Program at depths of 0, 5, 10, 20, 30, 40, 60, 80, 100, 120, 140, 160, and 180 m (see McIntire et al., 2007 for productivity methods), for 1987–1990 and 1996–2018. Few productivity measurements were available during months of January (4), April (1), and May (3) over this period.

Long-term dissolved oxygen profiles were collected by the National Park Service (NPS) and Oregon State University (OSU). The NPS data were collected with Van Dorn bottles typically at 11 depths ranging from 0 to 550 m monthly during summer of 1983–2016. Titration of NPS samples was done by visual color change using a glass burette dropper. The OSU data were collected once annually with Niskin bottles at around 18 depths ranging 0 to 585 m in July–August of 1988–2005. Winkler titration of OSU samples was controlled digitally with a Pt electrode (Crawford and Collier, 2007).

Oxygen demand rate constants at the lake floor were determined from high-frequency (30 min) dissolved oxygen measurements over a one year period using an RBRcoda optical dissolved oxygen sensor. The sensor was located approximately 1 m above the sediments at 588 m water depth at site B mounted on the same rope mooring as the temperature sensors.

Historical and future climate data

Downscaled future climate data were used to assess potential climate change effects on the temperature and salinity profiles, and subsequent impacts to deep-water ventilation of Crater Lake. The University of Idaho provides GCM data from the Coupled Model Intercomparison Project 5 (CMIP5; Taylor et al., 2012) that are statistically downscaled using the Multivariate Adaptive Constructed Analogs (MACA) version 2 technique (Abatzoglou and Brown, 2012). Daily air temperature and wind speed data downscaled to a 4-km spatial resolution were used for the historical per-

iod of 1951–2005 and the future period of 2006–2099. The bounding coordinates designating the area over Crater Lake were 42.89613°N to 42.97946°N and 122.1472°W to 122.0639°W, and this region included nine MACA grid points (Fig. 1). The downscaled air temperature and wind speed from the nine grid points were averaged for each day to acquire daily time-series sets representing conditions at Crater Lake as simulated by twelve GCM configurations under two future greenhouse gas trajectories.

Twelve GCM configurations (from ten different centers) were available as MACA-downscaled time series from the University of Idaho; their downscaled outputs were used to bracket the uncertainty of future simulations of deep ventilation in Crater Lake. The 12 GCMs generally performed in the top half of models evaluated by Rupp et al. (2013), who provided an extensive comparison of the performance of 41 CMIP5 GCM configurations in the Pacific Northwest of the United States (Electronic Supplementary Material, Table S3.1). Additionally, two available Representative Concentration Pathways (RCP) were evaluated for each GCM configuration: 1) RCP4.5, which demonstrates moderate climate mitigation action and stabilized radiative forcing of 4.5 W m^{-2} by 2100 (Thomson et al., 2011); and 2) RCP8.5, which demonstrates continued heavy reliance on fossil fuels without climate mitigation, reaching a radiative forcing level of 8.5 W m^{-2} by 2100 (Riahi et al., 2011).

Having a spatial resolution of 4 km, the historical and future downscaled air temperature and wind speed data were representative of the region bounding Crater Lake but needed to be further bias-corrected to a finer local scale that was representative of lake surface conditions. The bias correction of air temperature was accomplished using the change factor, or delta, method (Diaz-Nieto and Wilby, 2005; Minville et al., 2008). The same approach has been successfully applied in previous works (Piccolroaz et al., 2018; Piccolroaz and Toffolon, 2018; Piccolroaz et al., 2021). The bias correction of wind speed was accomplished using a quantile mapping method (Panofsky and Brier, 1968). This bias-correction approach for the adjustment of wind speed and the change factor bias correction to air temperature were successfully applied in a previous study of Crater Lake (Wood et al., 2016) to which the reader is referred for further details.

Modifications to the 1DDV model

Deep ventilation in Crater Lake results from thermobaric instabilities (Crawford and Collier, 2007). Although in principle deep ventilation associated with thermobaricity is a complex physical phenomenon, previous attempts to simulate it by reducing the problem to a 1-dimensional, parameterized vertical energy budget specifically designed to account for the thermobaric effect provided satisfactory results. Therefore, in this study we used the 1-dimensional deep ventilation (1DDV) model that was originally developed to investigate deep mixing in Lake Baikal (Piccolroaz and Toffolon, 2013) and was successfully applied to quantify the expected effect of climate change on deep ventilation in Lake Baikal (Piccolroaz and Toffolon, 2018) and in Crater Lake (Wood et al., 2016). The modified source code, input, and output files are available at Wherry et al., 2023) and a brief description of the model is provided in the Electronic Supplementary Material (ESM Appendix S1).

The comparison between the results obtained with 1DDV and the one-dimensional lake model DYRESM (Imerito, 2014) obtained in a previous application to the case of Crater Lake (Wood et al., 2016) showed the inadequacy of the latter model and confirmed the suitability of the algorithms included in 1DDV to properly simulate deep ventilation in this lake. It is relevant to note that the assessment of the water column stability needed for the stabilization algorithm is based on the Chen and Millero (1986) equation of state which includes the dependence of density on depth and thus accounts for the thermobaric effect. This application of 1DDV incorporates the salinity-dependent terms of the equation of state as well. In addition to a general rewriting of the code, modifications compared to the previous applications to Lake Baikal and Crater Lake include the incorporation of the dilution and concentration effects of precipitation and evaporation into the surface boundary condition and the loss of salinity through seepage, thus enabling the simulation of salinity and its effect on density dynamically. The 1DDV model requires a minimum of external forcing input data: water temperature, wind speed, and wind duration (determined by the temporal resolution of the wind speed dataset) are the basic input data. Precipitation and evaporation were added in this application for simulating the salinity profile. In addition to measured inputs and optimizable model parameters, 1DDV requires a reference turbulent diffusivity profile for heat, salt and dissolved oxygen, hydrothermal heat and salinity fluxes along the water column, the hypsometric curve (the relation between depth and water volume) to determine the layer discretization, and initial temperature and salinity profiles.

Surface boundary conditions

The 1DDV model does not calculate the surface heat balance; rather, lake surface water temperature (LSWT) in a 1-m thick surface layer is supplied as the surface boundary condition for solving the temperature profile (ESM eq. S1.1; the boundary conditions and reaction terms of the model are summarized in Table ESM Table S3.2). The time series of LSWT in the top 1 m was obtained from the downscaled and bias-corrected air temperature available from GCM outputs, by applying the *air2water* model (Piccolroaz, 2016; Piccolroaz et al., 2013). The *air2water* model is a simple hybrid model to predict LSWT based on air temperature solely, which based on several past applications has been proven to be a robust and reliable tool to hindcast and forecast LSWT with similar accuracy as more complex models that tend to require greater data inputs. The *air2water* model was run using the Crank-Nicolson solver for the full 8-parameter version, with the root-mean square error between observed and simulated LSWT as the objective function.

The surface boundary condition for the salinity model is the salt concentration resulting from dilution or concentration of salinity in the model upper layer (1.89 m thick with constant-layer volume of 0.1 km^3) based on the amount of precipitation and evaporation occurring at the surface in proportion to a constant surface-layer volume. Monthly average rates of precipitation were calculated from the long-term record collected at the Crater Lake National Park Headquarters weather station (National Weather Service cooperative station ID 35–1946) over 1931 to 2013. Based on these monthly averages, the long-term annual average rate of precipitation at Crater Lake is 169 cm yr^{-1}, which is consistent with other studies (Collier et al., 1990).

Monthly average evaporation rates from 1950 to 1996 were estimated by Redmond (1990) (ESM Table S3.3). Because of the small catchment area of the lake the volume responds rather directly to decadal precipitation and evaporation cycles, but otherwise is in a long-term balance with losses through seepage (the surface elevation varied by about 5 m over the century between 1890 and 1990 [Redmond, 1990] which is 1.4% of the total volume of the lake). For this study, therefore, the lake surface elevation and volume were assumed constant. Under that assumption, a closed water budget based on values in ESM Table S3.3 implies a seepage rate of about 97 cm yr^{-1} which converts to a flow rate of 1.68 m^3 s^{-1} of flow out of the system through the sediment–water interface area of the lake, less than but similar in magnitude to the previous estimate of 2.1 m^3 s^{-1} provided by Redmond (1990).

No long-term records of salinity that could be used to investigate the possibility of a trend over decadal time scales are available, and Nathenson (1990) concluded that the available data were "most easily" explained by a steady-state chemical balance in the lake. In the absence of evidence of long-term historical changes in salinity, it was considered most important to be able to attribute any changes in salinity in the future climate simulations to the changes in mixing induced by changes in climatic forcing. Consequently, the seepage, which is a loss term for salinity but does not enter the water mass balance, was treated as a calibration parameter for salinity and adjusted such that there was no long-term trend in the total salt content of the lake. The seepage was applied equally over 12 months and over the entire bottom area of the lake. For the same reason of attributing future changes in salinity to future changes in mixing rather than changes in the surface boundary condition, the long-term historical averages of precipitation and evaporation are used in future climate simulations rather than projecting changes in the ratio of those processes.

The surface boundary condition for dissolved oxygen was to set the surface layer concentration to 100 percent saturation (ESM Table S3.2).

Hydrothermal inputs

The summer temperature profile in Crater Lake has a temperature minimum (T_{min}) at a depth z_{min} below the seasonal thermocline, located generally between 250 and 350 m depth. The small increase in temperature with depth below z_{min} is a consequence of hydrothermal inputs (McManus et al., 1992) that determine the bottom boundary conditions for temperature and salinity (ESM Table S3.2). The hydrothermal heat flux was calculated from the change in heat content in the deep lake (below 350 m) from July to September for the 1990 to 2013 period, resulting in an average hydrothermal flux of 1.4 W m^{-2} (Wood et al., 2016), consistent with previous estimates of 0.9–1.2 W m^{-2} (McManus et al., 1993) and 0.7–1.4 W m^{-2} (Williams and Von Hertzen, 1983), which were based on fewer years of data. In this study the hydrothermal salinity flux was calculated analogously using the 1-m increment CTD profiles collected in the summer months over 1990 to 2016. For each year, salinity concentrations were converted to total mass in the lake and the change in mass, accounting for the seepage loss, was calculated over 1-month periods. The hydrothermal salinity flux was determined by assuming the net positive change in mass was attributable to inputs from the deep lake thermal vents below 350 m, which resulted in an average rate (over the 15 years for which adequate profiles were available for the calculation) of 0.012 ± 0.007 mg m^{-2} s^{-2}, about twice the previous estimate of 0.005 ± 0.003 mg m^{-2} s^{-2} (McManus et al., 1993). This previous estimate was based on two years of data and did not explicitly account for seepage, so the updated value reported herein was considered a better estimate and was used in the model.

Turbulent diffusion

The reference turbulent diffusivity profile required by the model to simulate temperature was determined using the heat budget method (Jassby and Powell, 1975; Powell and Jassby, 1974; Sweers, 1970). The interested reader is referred to Wood et al. (2016) for the details of how this was done. The profile reported in Wood et al. (2016) was projected onto the layer structure of the revised 1D model. The resulting profile (Fig. 2) shows an increase in diffusivity in the deep lake below the temperature minimum, where hydrothermal inputs make the water column marginally stable, and is broadly consistent with the previous estimates of a turbulent diffusion coefficient between 10^{-4} and 10^{-3} m^2 s^{-1} (McManus et al., 1993). The reference turbulent diffu-
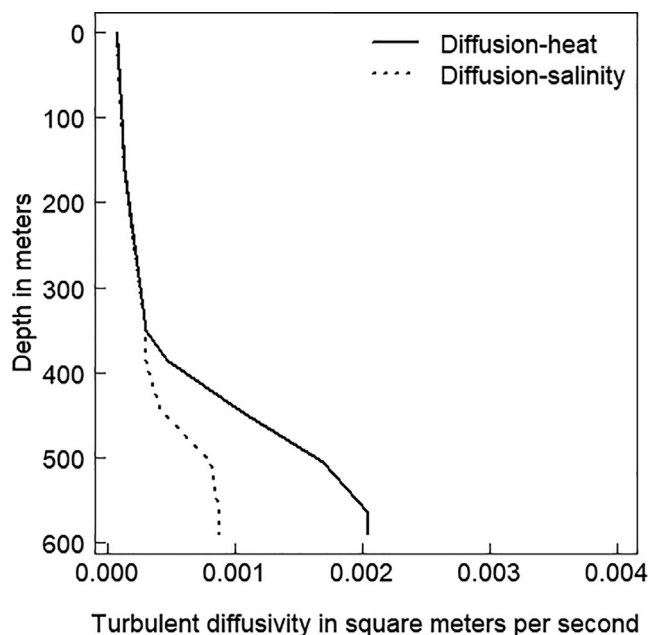

Fig. 2. Reference turbulent diffusivity profiles for temperature and salinity.

sivity profile for salinity was calculated from the salinity profiles using a budget method in an analogous manner (ESM Appendix S1).

The reference turbulent diffusivity profile for salinity determined in this way was similar to that for heat in the upper 350 m of the lake where heat and salinity are stably stratified, and the same curve was used for both profiles. However, the turbulent diffusivities for salinity were 36–60% less than that for temperature in the deep lake below 350 m (Fig. 2).

The diffusivity profile obtained for temperature and salinity were used as reference and updated at each computational time step by accounting for the stabilizing effect of thermal stratification and enhanced diffusion due to wind and other mixing processes, as described in Piccolroaz and Toffolon (2013, 2018). Specifically, the 1DDV model adjusts the reference diffusivity profile according to widely used Richardson number-based empirical relationships (Munk and Anderson, 1948; Pacanowski and Philander, 1981) and includes surface mixing processes due to wind and convection by modifying the diffusivity within the upper, well-mixed layer according to well-tested parameterizations (Gu et al., 2013; Subin et al., 2012; Xiao et al., 2016). To account for possible exceptional wind events, the reference diffusivity profile was assumed as the maximum between the one calculated based on a budget method and that obtained by the wind-based formulation proposed by Henderson-Sellers (1985). The reference diffusivity profile for temperature also was used for dissolved oxygen.

Dissolved oxygen rate constants

The source/sink term in the diffusion–reaction equation (ESM eq. S1.1, Table S3.2) for dissolved oxygen is composed of (1) volumetric losses, primarily due to decay of detrital material (DEC), and (2) volumetric net production from photosynthesis in excess of respiration (NPP, ESM Table S3.4). A second volumetric loss is oxygen consumption resulting from the oxidation of reduced elements that enter the lake with the hydrothermal fluids, specifically Fe, Mn, CH_4, and H_2S. The oxidation of reduced elements probably accounts for <2% of the oxygen demand (McManus et al., 1996).

Previous work provides some constraints on DEC. McManus et al. (1996) estimated DEC based on the change in oxygen content between sequential oxygen profiles. They determined that the total consumption of O_2 was in the range 2.4 to 2.9 mmol O_2 m^{-2} d^{-1} (77 to 93 mg O_2 m^{-2} d^{-1}) and occurred primarily below 300 m depth. Values of NPP are provided by McIntire et al. (2007) in terms of carbon, based on a shorter record of the ^{14}C data we use below. McIntire et al. (2007) found that primary production was limited to the top 180 m of the water column, generally peaked between 60 and 120 m depth, and had a large interannual variability. Maximum volumetric production of C in the water column profile was generally between about 0.4 to 0.6 mg C m^{-3} hr^{-1}. Using a stoichiometric relation to represent photosynthesis (6 molecules of O_2 created for every 6 C atoms in glucose created by the reaction; Bowie et al., 1985) this converts to a maximum volumetric rate of oxygen production of 0.013 to 0.019 mg O_2 L^{-1} d^{-1} (using a 12-hour photoperiod). Urbach et al. (2001) measured a maximum primary productivity of 167 ng C L^{-1}h^{-1} (0.17 mg C m^{-3} hr^{-1}) at 120-m depth, which can be converted a to volumetric oxygen production of 0.006 mg O_2 L^{-1} d^{-1}.

NPP was calculated as follows. The primary production data determined with ^{14}C were converted from units of mg C m^{-3} hr^{-1} to units of mg O_2 L^{-1} d^{-1} using stoichiometry (Bowie et al., 1985), which resulted in a ratio of 2.67 mg O_2 to mg C. The data were then compiled by month and aggregated by depth into 3 groups: 0 to 50 m (includes measurements at 0, 5, 10, 20, 30 and 40 m), 50 to 100 m (includes measurements at 60, 80 and 100 m), and 100 to 180 m (includes measurements at 120, 140, 160 and 180 m). The values were weighted by the volume of the lake layer represented by the measurement, and an average for the 3 depth ranges was the final NPP rate throughout the entire range. Monthly averages of the data were used for months when data were collected, and a linear interpolation between surrounding months was used for February, March, October, November and December (ESM Table S3.4). The monthly values were then multiplied by the average photoperiod for the month (Forsythe et al., 1995) as calculated with the R package meteor (v0.3–4; Hijmans, 2019). The monthly values are in the range of 3×10^{-4} to 0.0231 mg O_2 L^{-1} d^{-1}, within the range found by McIntire et al. (2007) using the shorter dataset, and bracketing the maximum value found by Urbach et al. (2001).

Oxygen consumption from the decay of detritus (DEC) was determined using the time series of dissolved oxygen concentration collected near the bottom of the lake at site B between July 2018 and July 2019. A linear regression line was fit to sections of the data between July 3, 2018 (when the instrument was installed) through October 15, 2018, and between April 15 and July 10, 2019 (when the instrument was removed). These sections of the data were least affected by other advective and mixing processes (Fig. 3). The rate of decay during the late summer of 2018 was more than 3 times the decay during the spring of 2019 (4.53×10^{-3} mg O_2 L^{-1} d^{-1} and 1.40×10^{-3} mg O_2 L^{-1} d^{-1}, respectively). The spring value is close to the high end of a previous estimate of 0.4 to 0.44 µmol L^{-1} d^{-1} (1.28×10^{-3} to 1.41×10^{-3} mg O_2 L^{-1} d^{-1}) for the water column at 550 m depth (McManus et al., 1996). McManus et al. (1996) estimated consumption at 300, 450 and 550 m depth. They calculated that O_2 consumption at 450 m was about 40% of that at 550 m, and at 300 m they estimated that there was no excess oxygen consumption. We used an average of the two rates obtained by linear regression (2.97×10^{-3} mg O_2 L^{-1} d^{-1}) to represent annually averaged DEC at 550 m depth. The rate increased with depth linearly from 0 at 375 m depth to 2.97×10^{-3} mg O_2 L^{-1} d^{-1} at 550 m depth and continued to increase at the same linear rate to the maximum depth. The value of DEC calculated this way at 450 m was 1.27×10^{-3} mg O_2 L^{-1} d^{-1}, about 43% of the value at 550 m, roughly consistent with

the depth relation found by McManus et al. (1996). This linearly increasing DEC rate resulted in a total areal consumption rate of 94 mg O_2 m^{-2} d^{-1} below 300 m, the upper end of the range of values for oxygen consumption provided by McManus et al. (1996).

An additional loss term for dissolved oxygen that is important in some lakes is the demand at the sediment–water interface. The dissolved oxygen profiles do not provide strong evidence of oxygen consumption above the background water-column DEC rate that would be associated with the decay of material at the sediment–water interface (McManus et al., 1996). The recycling efficiency of particulates sinking from the upper water column was estimated to be between 85 and 95% (Dymond et al., 1996; Fennel et al., 2007), indicating that little of the detrital material sinking from above is deposited on the bottom and the sediments likely have a small organic fraction. McManus et al. (1996) noted that hydrothermal fluid input results in lower oxygen concentration in the near-bottom waters of the south basin relative to the east basin where site B is located, but they argued that this is largely because the hydrothermal fluids make the near-bottom waters of the south basin more resistant to ventilation and therefore the residence time is longer. This effect is likely to be localized to the vicinity of the source of hydrothermal fluids and is not primarily a result of enhanced oxygen demand at the bottom. Given that most of the oxygen demand from the decay of detrital material occurs within the water column and is incorporated into the DEC rate constant estimated here, and lacking good estimates of the sediment oxygen demand, that term is considered small and set to zero in this application of the model.

Assessment of model performance

The 1DDV model was run over the complete 21-year period covering July 10, 1992 to July 8, 2013 and calibrated to the 6-year period covering September 23, 2000 to August 3, 2006. Validation was considered for the 15-year period covering July 10, 1992 to September 22, 2000 and August 4, 2006 to July 8, 2013. Model performance was evaluated using bias, root-mean-square error (standard deviation of the errors, RMSE), the unitless normalized root-mean-square error (RMSE divided by the range of the data, NRMSE) and the coefficient of variation of the root-mean-square error (RMSE divided by the mean of the data, CVRMSE).

Definition of deep ventilation events

Deep ventilation events occur in a continuum from small to large in terms of the volume of deep water replaced and the decrease in deep lake heat content and temperature at the thermistors. It is useful to separate Crater Lake into an upper water column (UWC) and lower water column (LWC) at 350 m, approximately where the minimum in the temperature profile occurs, and approximately the depth below which convective mixing in the spring and fall does not reach (McManus et al., 1993; Crawford and Collier, 2007). To determine the frequency of wintertime deep ventilation, we defined the occurrence of a deep ventilation event to be when the minimum LWC heat content in spring (identified within the time window from February to June) was less than the maximum LWC content in the preceding winter (identified within the 6-month window preceding the spring minimum) by more than 0.5×10^6 GJ. A decrease in heat content in the LWC above this threshold was attributed to replacement of some significant fraction of the LWC with water from the UWC at a lower temperature and was used to identify a winter in which deep ventilation occurred. This threshold is consistent with estimates of the volume associated with ventilation events (Crawford and Collier, 1997). Setting the threshold at this value resulted in frequencies of deep ventilation during the historical period of about
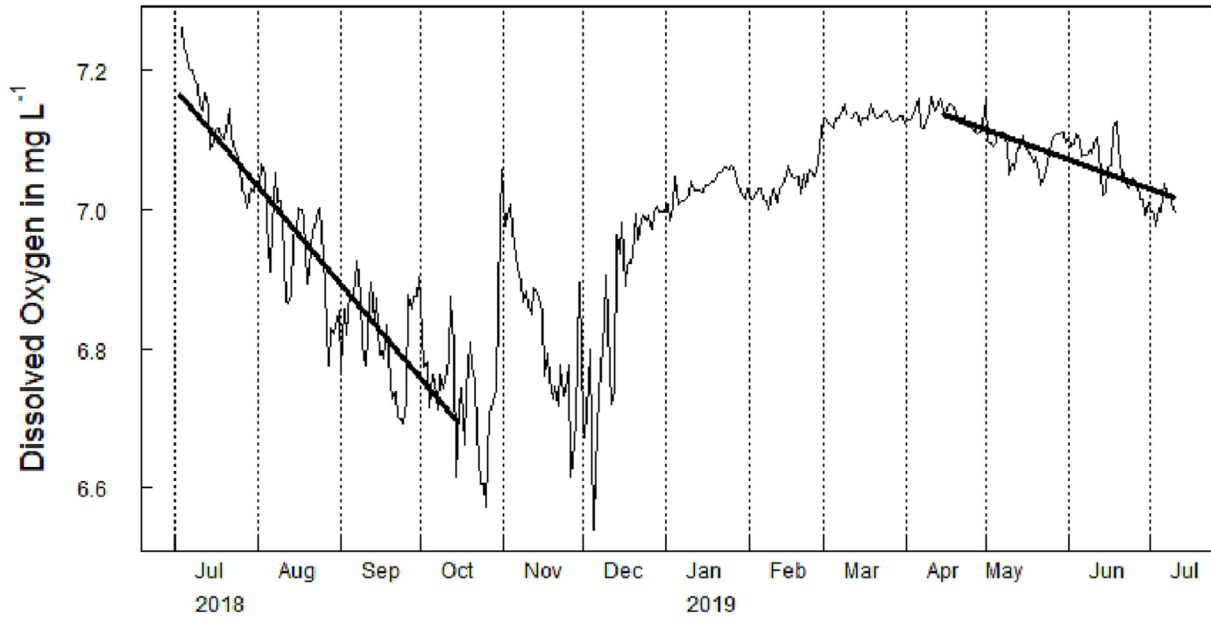
Fig. 3. Near-bottom time series of dissolved oxygen, and linear regression used to calculate the rate of volumetric loss.

five winters per decade, which corresponds to the estimates of mixing frequency that have been made based on temperature and salinity profiles (Crawford and Collier, 2007; McManus et al., 1993) and estimates of the residence time of chlorofluorocarbons (Weiss, 1992).

Sensitivity of lake stability to the salinity gradient

The stability of the density gradient in the upper and lower lake was determined by calculating the average buoyancy frequency between two depths:

$$N^2 = -\frac{g}{\bar{\rho}}\left(\frac{\rho_{z1} - \rho_{z2}}{\Delta z}\right) \tag{1}$$

where $\rho_z = \rho(T_z, S_z)$; T_z, S_z are the simulated profile values of temperature and salinity, respectively, and $\bar{\rho}$ is the average density between z_1 and z_2. To investigate the contribution of the temperature and salinity profiles separately, N^2 was calculated using the vertical temperature gradient only:

$$N_T^2 = -\frac{g}{\bar{\rho}}\left(\frac{\rho_{T,z1} - \rho_{T,z2}}{\Delta z}\right) \tag{2}$$

where $\rho_{T,z} = \rho(T_z, \bar{S})$, and using the salinity gradient only:

$$N_S^2 = -\frac{g}{\bar{\rho}}\left(\frac{\rho_{S,z1} - \rho_{S,z2}}{\Delta z}\right) \tag{3}$$

where $\rho_{S,z} = \rho(\bar{T}, S_z)$, and $\bar{T}$ and $\bar{S}$ are the average temperature and salinity between z_1 and z_2. We ignore the adiabatic temperature gradient correction to N_T^2 because the in-situ temperature gradient greatly exceeds the adiabatic gradient.

Sensitivity of deep ventilation to the salinity gradient

The sensitivity of the frequency and depth of deep ventilation to the salinity gradient was investigated by counting the number of days in the simulation when density conditions were favorable for initiating thermobaric instability, and then determining how varying the salinity profile changed that count. To do this, the dif-

ference between the in-situ density at 300 m and the potential density at 300 m of a water parcel originating from 100 m was defined as $\Delta\rho\prime_{300} = \rho_{300} - \rho_{\theta,300}$ where $\rho_{\theta,300} = \rho(T_{100}, S_{100}, P_{300})$ and similarly, the difference between the in-situ density at 550 m and the potential density of a water parcel originating from 100 m was defined as $\Delta\rho\prime_{550} = \rho_{550} - \rho_{\theta,550}$ where $\rho_{\theta,550} = \rho(T_{100}, S_{100}, P_{550})$.

We evaluated $\Delta\rho\prime_{300}$ in the output of one randomly selected GCM, RCP8.5 scenario, and selected the set of days $\{t_{tb}\}$ one time step prior to a first occurrence of $\Delta\rho\prime_{300} < 0$, which indicated an unstable water column and the start of a mixing event. The threshold value for $\Delta\rho\prime_{300}$ that would indicate potentially favorable (depending on other factors, weather in particular) conditions for thermobaric instability was defined as the median value of $\Delta\rho\prime_{300}$ over $\{t_{tb}\}$, designated $(\Delta\rho\prime_{300})_{thr}$. We then counted all the days in the first and last 55-year period when $0 \le \Delta\rho\prime_{300} \le (\Delta\rho\prime_{300})_{thr}$, indicating the potential for thermobaric instability (NPTI).

To evaluate the contribution of the salinity gradient to NPTI, a uniform profile was defined as $S_u = 100$ mg L^{-1} at all depths. To test the sensitivity of NPTI to error in the salinity gradient, a "weak" profile that incorporated our best estimate of potential bias in the simulated profile was defined as $S_{wk} = S_{sim} \times (S_{obs}/S_{cal})$, where S_{sim} is the time-varying simulated salinity profile, S_{obs} is the average of measured profiles during the calibration/validation period, and S_{cal} is the average of the simulated profiles that corresponded to the measured profiles. The density difference $\Delta\rho\prime_{300}$ was re-calculated using S_{wk} and S_u, and the NPTI obtained in each case was compared to the value obtained with S_{sim} to determine the sensitivity of NPTI to the salinity gradient. To evaluate the importance of a dynamic as opposed to static salinity, NPTI also was calculated with the S_{obs} salinity profile, constant in time.

The value of $\Delta\rho\prime_{550}$ during days when $0 \le \Delta\rho\prime_{300} \le (\Delta\rho\prime_{300})_{thr}$ is an indication of whether a ventilating volume from 100 m has the potential to descend to 550 m or will stop at some point above the bottom. If $\Delta\rho\prime_{550}$ is negative, then ventilation could occur as deep as 550 m; if it is positive, then ventilation will not make it to the bottom of the lake. The number of days that the two conditions, $\Delta\rho\prime_{550} < 0$ and $0 \le \Delta\rho\prime_{300} \le (\Delta\rho\prime_{300})_{thr}$, were met (NBV) was compared among calculations of $\Delta\rho\prime_{550}$ using S_{sim}, S_u, S_{wk}, and S_{obs}, as

a measure of the sensitivity of the depth of ventilation to the salinity gradient, potential bias in the salinity gradient and to a dynamic, as opposed to static, salinity.

Results

Calibration and validation of temperature and salinity

The 1DDV model was run over the complete 21-year period covering July 1992 to July 2013 and calibrated to the period covering September 2000 to August 2006. The rest of the 21-year period was used for validation. Values of ξ, η and the mixing coefficient were adjusted to optimize the error statistics for the temperature time series at 16 depths (ESM Table S3.5) and the overall heat content in the lake above and below 350 m. The final combination of parameter values that minimized the average NRMSE for deep-lake heat content, while also providing the best simulations of temperature time series between 20 and 580 m was: ξ equal to 28 kg m^{-2} s^{-1}, η equal to 0.019 km h, and the mixing coefficient equal to 0.27%.

The resulting calibrated model accurately captured reverse stratification occurring in winter months with a realistically thick mixed layer as much as 200 m deep in some years (ESM Fig. S2.1). The model had a tendency to simulate colder temperatures than measured in the metalimnion down to 200 or 250 m depth in late spring and summer (ESM Fig. S2.2), but these biases were small as indicated by the small statistical bias in the time series across 16 depths (maximum 0.1 °C at 350 m), and the RMSE that varied from a maximum of 0.5 °C at the surface to a minimum of 0.09 °C at 250 m (ESM Table S3.5). Overall, the simulations capture the temperature profile through the whole water column, as well as seasonal changes. The comparison between simulated profiles and the periodic CTD temperature profiles provided an additional validation of the temperature modeling (Fig. 4). Error statistics were comparable to those calculated for the temperature time series above 200 m (where most of the profile measurements are made), across the calibration and validation periods (ESM Table S3.6).

The model performance in simulating salinity was evaluated by comparing the CTD profiles to model profiles (Fig. 4). The bias and RMSE across 105 salinity profiles were small (-0.02 mg L^{-1} and 0.4 to 0.7 mg L^{-1}, respectively), and the NRMSE (0.02–0.06) was similar to that for the temperature profiles (0.03, ESM Table S3.6). The overall bias in the profiles was small, indicating that the total amount of salt in the water column was simulated accurately. When the measurements above and below 350 m depth were considered separately; however, there was an overall bias of −0.13 to −0.2 mg L^{-1} above 350 m (about 77% of the lake volume), and 0.40 to 0.61 mg L^{-1} below 350 m (Fig. 4), which appears in some of the profiles as a stronger gradient in the simulations than in the observations between about 200 m and the lake bottom (ESM Fig. S2.3). The most straightforward explanation would be that seepage occurs primarily in the deep lake, whereas we distributed the total seepage across all the bottom area evenly. The implications of this potential bias for initiating deep ventilation and the depth of deep ventilation are discussed with the results of future simulations.

Because the purpose of this study was to evaluate changes in the frequency of deep ventilation, it was important to demonstrate that the model simulated deep ventilation events in the calibration/validation period with the observed frequency. We identified 11 years in the calibration/validation period during which deep ventilation occurred over the winter, based on visual inspection of the lake temperature time series at 530 m (ESM Fig. S2.2) and the deep lake heat content time series (ESM Fig. S2.4). The model simulated deep mixing in 9 of these 11 years, and in 2 additional

years. A deep mixing event triggered by thermobaric instabilities resets bottom temperature and salinity to lower values but does not create a uniform vertical profile. This can be seen in the contour plots of measured and simulated temperature (ESM Fig. S2.1) and salinity (ESM Fig. S2.5) and shows the ability of the 1DDV model to simulate the 3-dimensional process in one dimension. Overall, the frequency of deep ventilation as indicated by drops in temperature and heat content was simulated accurately in the calibration/validation period with an annual occurrence rate of 0.52.

Calibration of steady state salinity

Seepage was calculated to ensure that no long-term changes in the salinity content of the lake were simulated during the historical period, so that any long-term changes found in the future climate simulations could be attributed only to changes in the future mixing regime. The 1DDV model was run with the calibrated parameters for a randomly selected GCM over the historical period of 1950–2005, and the seepage was adjusted by trial and error to 1.88 m^3 s^{-1} to maintain a seasonally varying salinity content with no long-term trend over the 55-year simulation. This was determined by fitting a linear regression to the daily values of total salt content (integrated over entire water column) for the 55-year historical period and verifying that the slope was neither increasing nor decreasing with statistical significance. The performance statistics during the calibration and validation period were unchanged, and the model was considered calibrated and validated for the period of observed record and ready to use with the GCM configurations and scenarios.

Dissolved oxygen validation

Our purpose in simulating dissolved oxygen concentration is to evaluate the expected magnitude of the effect that long-term changes in the frequency of deep ventilation will have on profundal dissolved oxygen concentration. Therefore, it was important for the simulation of dissolved oxygen to obtain a good calibration of temperature and salinity, the variables that determine the occurrence of the conditions that initiate deep ventilation, and to demonstrate that the model correctly simulated the frequency of deep ventilation during the time frame of observations, as described above. The limited availability of dissolved oxygen observations did not support a robust calibration of that variable, and therefore no model parameter was adjusted to optimize error statistics for the simulation of dissolved oxygen.

Once the calibration of temperature and salinity was completed, however, the model performance in simulating dissolved oxygen (DO) was evaluated by comparing 73 measured DO profiles to model profiles (Fig. 4 and ESM Fig. S2.6). The simulated DO profiles correctly captured the surface minimum concentrations, subsurface maximum concentrations at about 100 m depth, and decreasing concentration from 100 m to the bottom of the lake. The subset of profiles shown in ESM Fig. S2.6, all collected in mid-September, suggest a systematic positive bias in the simulations. The error statistics confirm a positive bias across the 73 profiles collected by NPS throughout the year—the bias, RMSE and NRMSE were 0.39 mg L^{-1}, 0.78 mg L^{-1} and 0.15, respectively. The agreement with the OSU profiles (13 profiles) was systematically better (bias, RMSE and NRMSE of 0.15 mg L^{-1}, 0.49 mg L^{-1} and 0.17, respectively), as indicated in Fig. 4, but we do not currently have a basis for assessing the relative accuracy of these two measurements. Crucially for our purpose, the bias in the simulations does not appear to increase through the years. This suggests that while our calculated production rates may be too high and/or our calculated decay rate too low, the two are in a dynamic
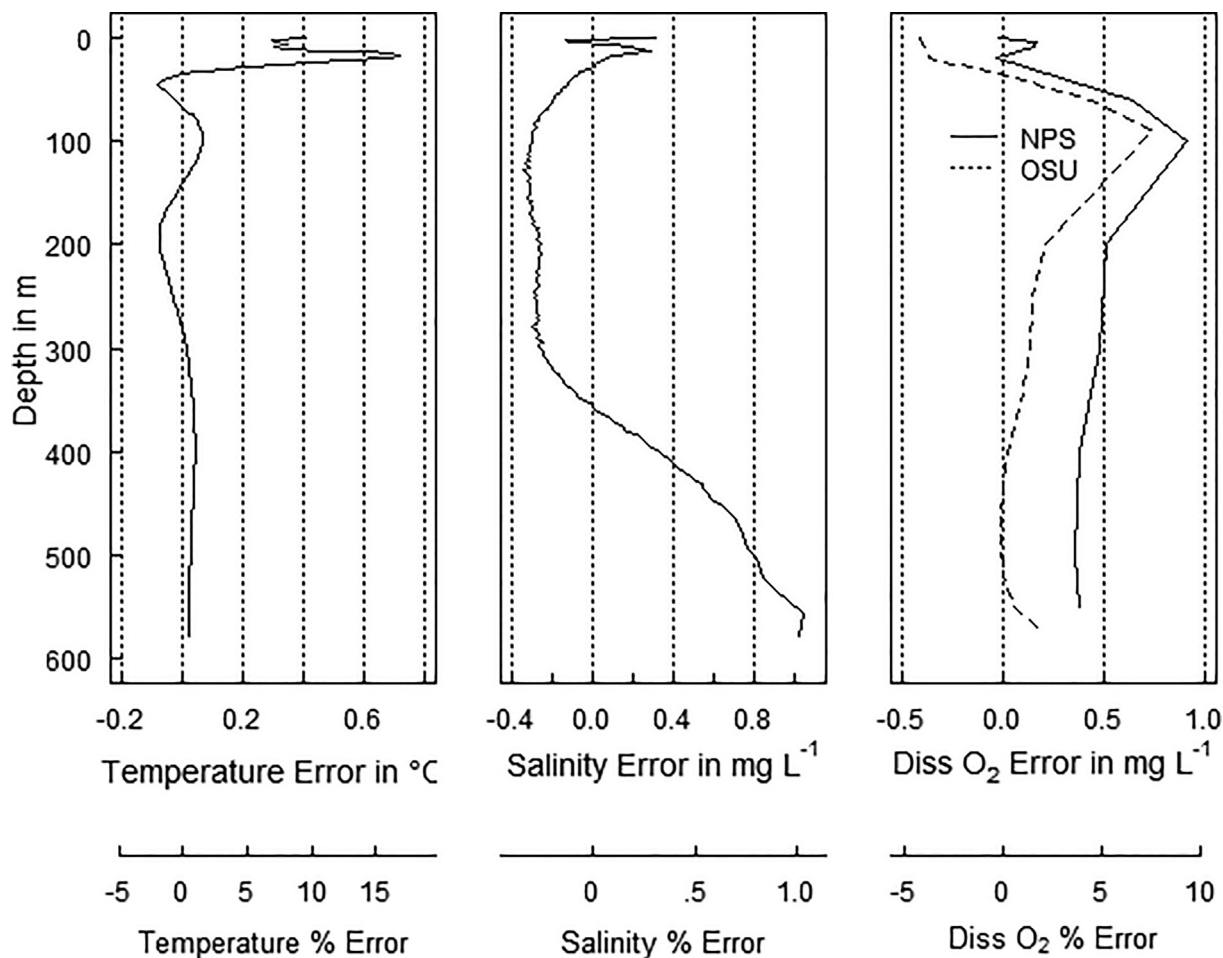
Fig. 4. The mean difference between profiles of temperature, salinity and dissolved oxygen concentration simulated with the calibrated 1DDV model, and profiles obtained from measurements with a CTD (temperature and salinity) or titration (dissolved oxygen). On the second axis, the mean difference is divided by the overall mean of the measurements, and converted to a percentage.

steady-state and the excess dissolved oxygen in the profiles does not accumulate through time, which would confound our ability to evaluate the long-term effects of a changing frequency of ventilation.

Future simulations

The rates of change in volumetrically averaged water temperature, salinity, and dissolved oxygen concentration were determined by linear regression modeling of results from each GCM and scenario, and three 55-year periods, for the UWC and LWC separately. These rates are summarized in Fig. 5. The 12-model ensemble averages are provided in ESM Tables S3.7-S3.9. The distribution of the annual averages from the 12 GCMs is shown as a time series in ESM Figs. S2.7 (water temperature), S2.8 (salinity), S2.9 (dissolved oxygen concentration) and S2.10 (dissolved oxygen percent saturation).

Temperature

The future climate temperature simulations show a large range in the water temperature trends simulated by the 12 GCMs, but the ensemble in its entirety shows clear increasing trends in temperature starting in the 21st century (Fig. 5 A,D and ESM S2.7, Table S3.7). Between 2006 and 2061, the ensemble mean temperature increased in the UWC by 0.07 (RCP4.5) and 0.09 (RCP8.5) °C

decade^{-1} (ESM Table S3.7). Between 2045 and 2099, the rate of change in air temperature slowed compared to 2006–2061 in the RCP4.5 scenario but accelerated in the RCP8.5 scenario (ESM Table S3.7). This divergence in air temperature trends led to a divergence in the water temperature trends in the RCP4.5 and RCP8.5 scenarios, particularly in the UWC. In 2045–2099, the ensemble mean temperature in the UWC increased at about the same 2006–2061 rate of 0.06 °C decade^{-1} in the RCP4.5 scenario, but the rate doubled compared to 2006–2061 to 0.18 °C decade^{-1} in the RCP8.5 scenario (Fig. 5A, ESM Table S3.7). In the LWC, the ensemble mean annual averaged temperature increased by 0.02 (RCP4.5) and 0.03 (RCP8.5) °C decade^{-1} between 2006 and 2061, and by 0.03 (RCP4.5) and 0.11 (RCP8.5) °C decade^{-1} between 2045 and 2099 (Fig. 5D, ESM Table S3.7). Generally, the rate of temperature increase in the LWC was between one third and one half that in the UWC between 2006 and 2099, but in the RCP8.5 scenario, the rate of temperature increase more than tripled between the year ranges 2006–2061 and 2045–2099 (ESM Table S3.7).

The 55-year trends smooth out high interannual variability within a single GCM. The CNRM-CM5 GCM results are highlighted in ESM Fig. S2.7, illustrating that one of the features of future temperature in the lake could be more extreme multi-year variability than characterized the 20th century. A contour plot of temperature from CNRM-CM5 shows a mid-water column minimum in temperature persisting throughout the timeline (Fig. 6). Wintertime
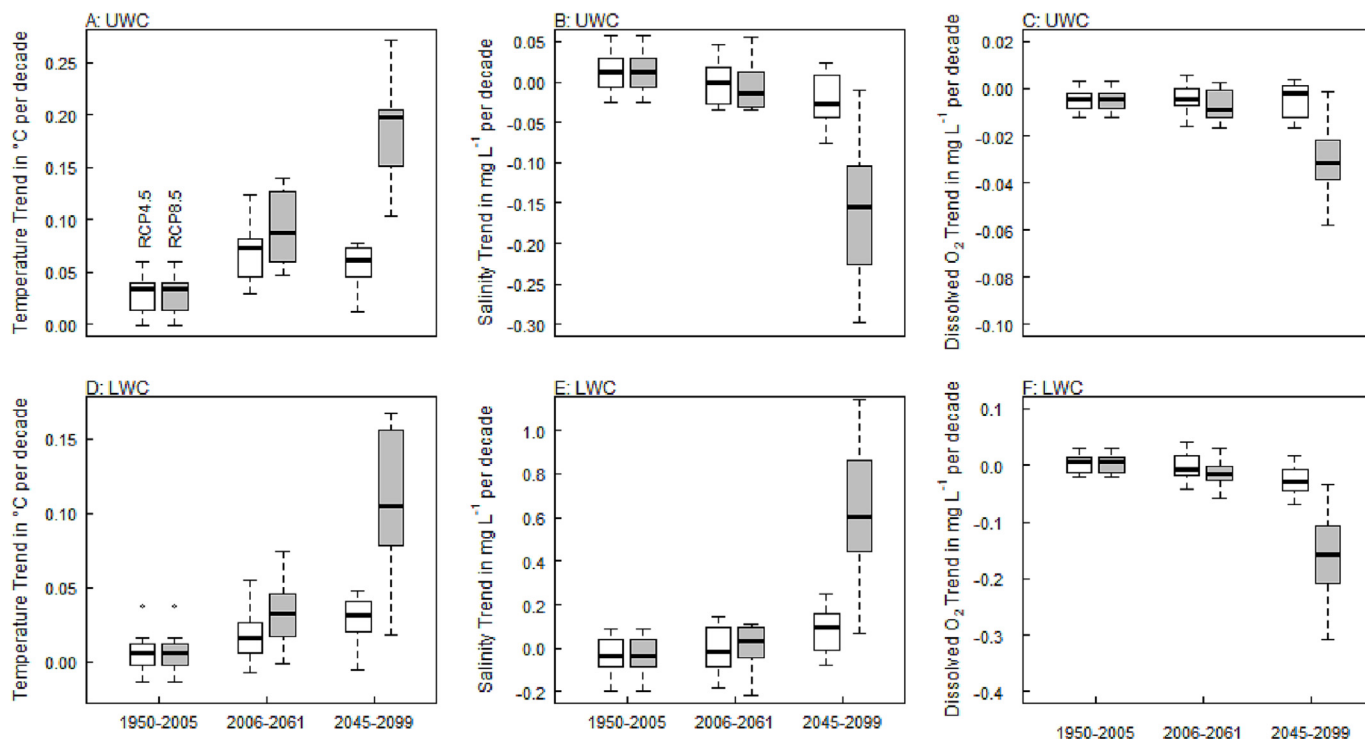
Fig. 5. Rates of change based on linear regression models of upper and lower water column annually averaged variables simulated by 1DDV model, over 3 55-year periods. The boxplots show the distribution of values from 12 climate models: A) water temperature, upper water column, B) salinity, upper water column, C) dissolved oxygen, upper water column, D) water temperature, lower water column, E) salinity, lower water column, F) dissolved oxygen, lower water column.
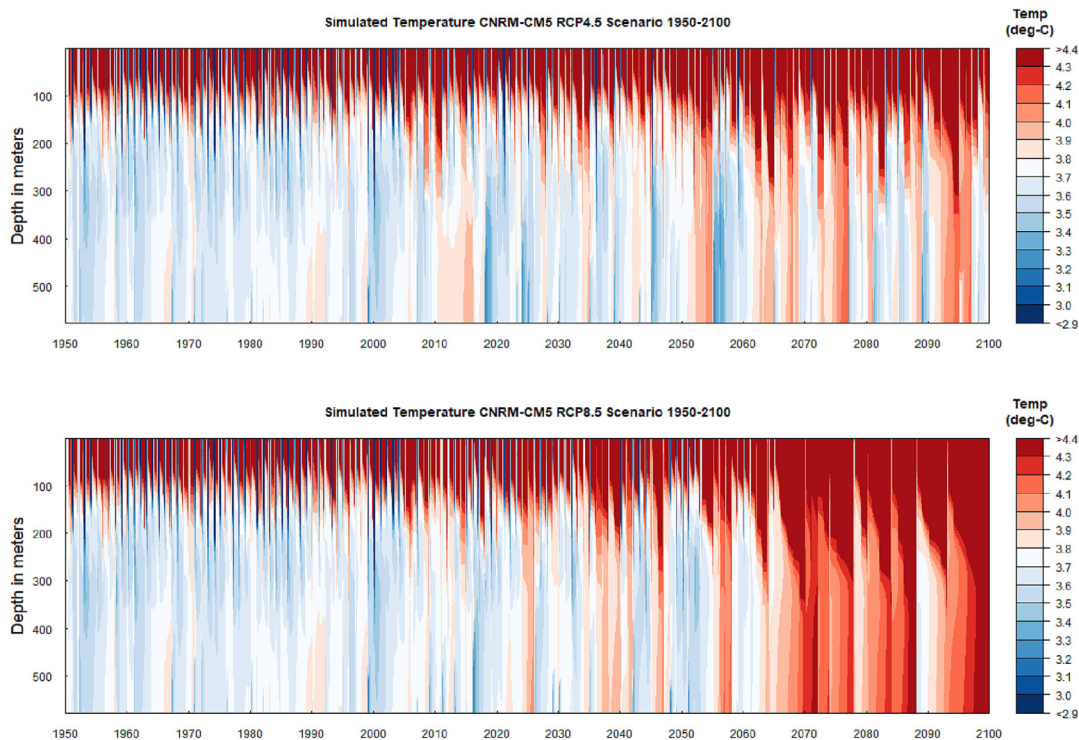

Fig. 6. Contours of water temperature simulated with 1DDV model, with lake surface temperature and wind forcing provided by the CNRM-CM5 GCM, 1950–2099, 2 emissions scenarios.

reverse stratification occurs less often starting about 2070 (RCP4.5) and 2050 (RCP8.5), at which time temperature approaching or above 4 °C becomes common throughout the water column. All the models were consistent with CNRM-CM5 in predicting that the necessary conditions to initiate deep ventilation will occur less often in the last half of the 21st century.

Salinity

The ensemble mean trends in salinity were small and less than the standard deviation in the models throughout the timeline in the RCP4.5 scenario (Fig. 5B, E; ESM Table S3.8) and through 2061 in the RCP8.5 scenario. The calibration of seepage ensured no long-term increase in the total salt content, and the simulations did not show a long-term redistribution of salt between the UWC and LWC through 2061 (ESM Fig. S2.8, Table S3.8). In the second 55 years of the future climate simulations, however, a clear upward trend was evident in the LWC, although there was a large range among the different GCMs and the trend was small in the RCP4.5 scenario (ESM Fig. S2.8). In the RCP8.5 scenario, between 2045 and 2099, the ensemble mean salinity increased by 0.64 mg L^{-1} decade^{-1} in the LWC and decreased by 0.16 mg L^{-1} decade^{-1} in the UWC (ESM Table S3.8), indicating a re-distribution of salt from the UWC to the LWC. Contours of salinity from a single GCM (Fig. 7) show the salinity profile steepening with each deep mixing event—higher salinities below 350 m reset to fresher values, and above 350 m salinity increases as water is exchanged with water from deep in the lake. The lower frequency of deep mixing events after 2050 is visually apparent in the CNRM-CM5 GCM, RCP8.5 contours (Fig. 7) as a progressively stronger gradient between higher maximum values at the bottom and lower minimum values at the surface between events that are less frequent.

Frequency of deep ventilation

The ensemble mean of the frequency of deep ventilation decreased between the baseline period (5.4 years every decade) and the first 55 years of future climate simulation (to 5.1 years every decade for both the RCP4.5 and RCP8.5 scenarios), and then decreased during the last 55 years of future climate simulation to 4.3 years every decade and 2.5 years every decade for the RCP4.5 and RCP8.5 scenarios, respectively (Fig. 8, Table 1). As the frequency of deep ventilation went down, the ensemble mean decrease in heat content during a winter in which deep ventilation occurred went up, from 2.71 × 10^6 GJ during the baseline period, to maximums of 5.29 × 10^6 GJ (+95%) and 6.24 × 10^6 GJ (+130%) during the last 55 years of the RCP4.5 and RCP8.5 simulations, respectively. The lower frequency of deep ventilation and the greater volume of deep-water replacement manifests in the time series of near-bottom temperature and salinity as a greater increase of temperature and salinity over longer times between events, punctuated by rapid drops in temperature and salinity when an event occurs (ESM Fig. S2.9).

Water column stability

Observations show that the salinity gradient within the LWC stabilizes the deep water column in which the temperature gradient would otherwise be unstable (McManus et al., 1993), and our simulations showed that this continued to be the case through
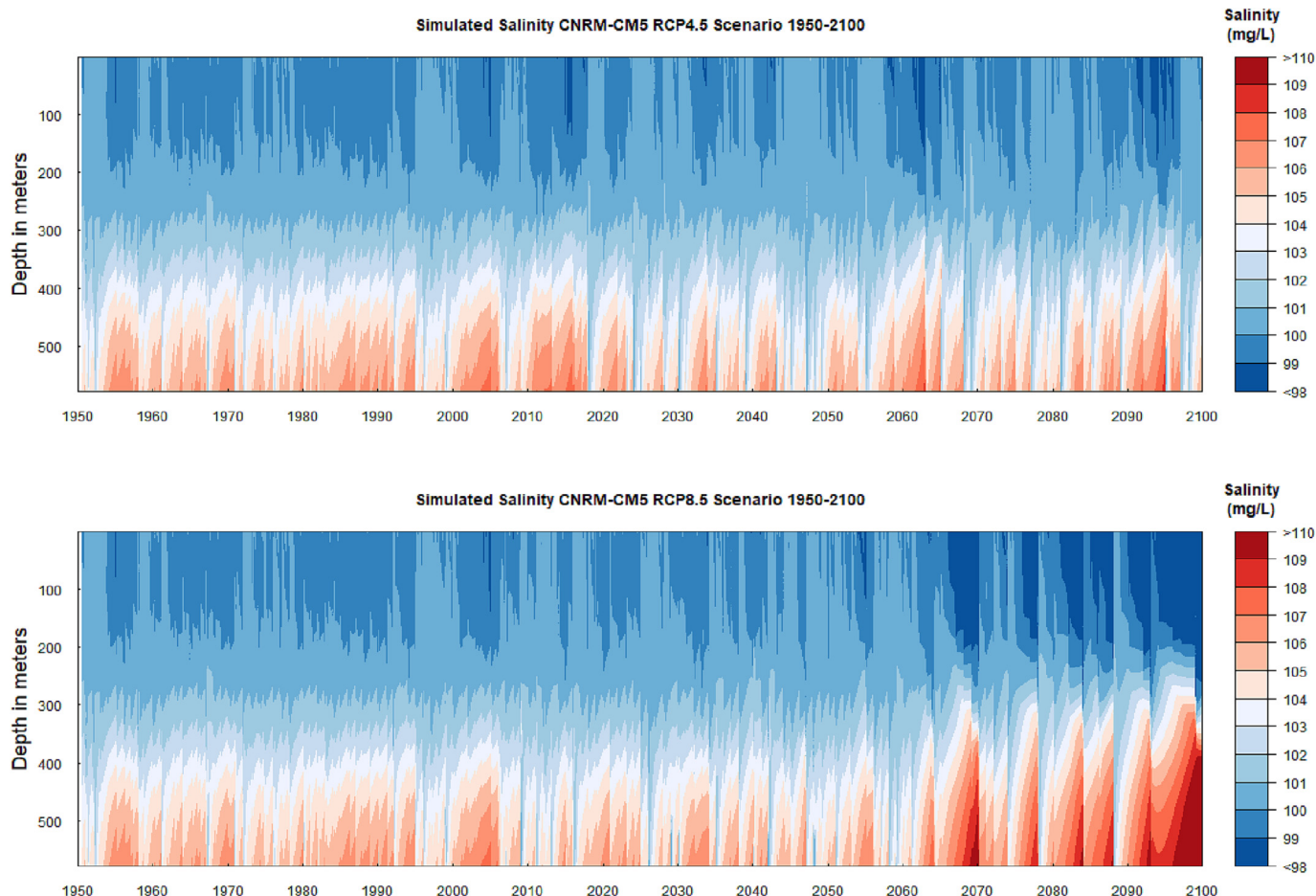

Fig. 7. Contours of salinity simulated with 1DDV model, with lake surface temperature and wind forcing provided by the CNRM-CM5 GCM, 1950–2099, 2 emissions scenarios.
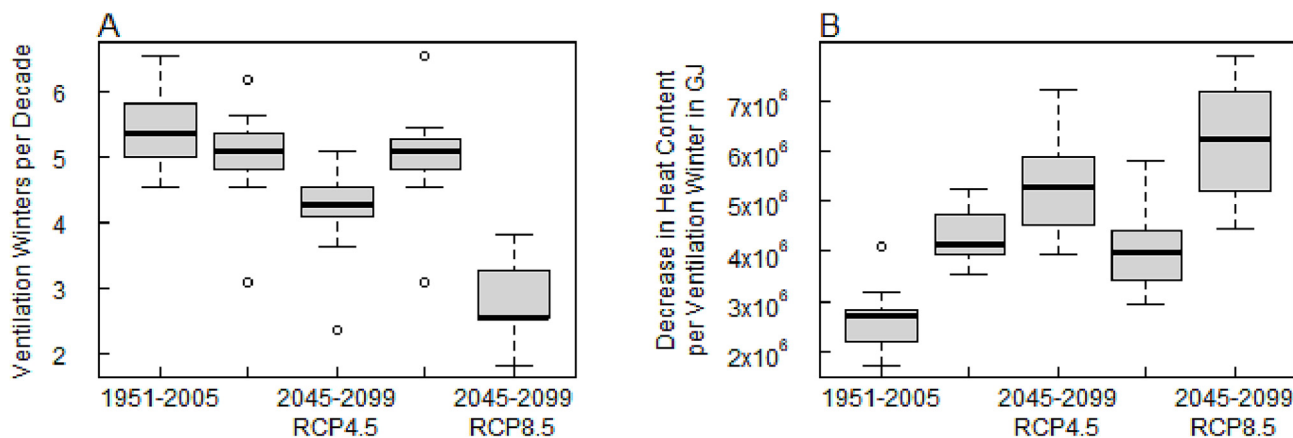
Fig. 8. A) Frequency of winters in which ventilation of deep water occurs over 3 55-year time periods and 2 RCP scenarios, ensemble of 12 GCMs. B) The decrease in heat content associated with ventilation events.

Table 1

Characteristics of wintertime deep ventilation (below 350 m depth), defined as a decrease in total heat content of at least 0.5×10^6 GJ from the winter maximum to the minimum the following spring. Values are the median of 12 general circulation models.

Period	Frequency of wintertime deep ventilation [number of winters decade^{-1}]	Mean drop in heat content each ventilation winter [x10^6 GJ]
Baseline, 1950–2005	5.4	2.71
RCP4.5, 2006–2061	5.1	4.12
RCP4.5, 2045–2099	4.3	5.29
RCP8.5, 2006–2061	5.1	3.96
RCP8.5, 2045–2099	2.5	6.24

2099. The contributions of the salinity and temperature gradients to the stability of the LWC were compared by means of the contribution of each to the average buoyancy frequency N^2 over 350 to 550 m (ESM Fig. S2.10A), focusing on winter conditions because that is the critical time frame for deep ventilation. From the CNRM-CM5 GCM, the average winter N_S^2 was notably consistent at 1.2–1.3×10^{-7} s^{-2}. These values easily exceeded values of N_T^2, which increased slightly through time from -2.0×10^{-9} s^{-2} in 1950–2005 to -1.0×10^{-8} s^{-2} in 2045–2099. Aside from episodic mixing events, in our simulations the salinity gradient in the LWC was positive and dominated the negative (unstable) temperature gradient through 2099.

The evolution through time of N^2 in the UWC was quite different. The buoyancy frequency was calculated over 100 to 300 m depth, again focusing on winter conditions. N^2 increased by nearly an order of magnitude from an average of 1.7×10^{-7} s^{-2} in 1950–2005 to 1.3×10^{-6} s^{-2} in 2045–2099. The increase in N^2 was dominated by the contribution of the temperature gradient, which increased throughout the timeline (ESM Fig. S2.10B), especially after 2050 when wintertime reverse stratification was nearly eliminated.

Sensitivity of deep ventilation to the salinity gradient

The results from the CNRM-CM5 GCM, RCP8.5 scenario, were used to investigate the sensitivity of the estimated deep ventilation frequency to the possible errors in simulating the salinity profile. The threshold value $(\Delta \rho'_{300})_{thr}$ for screening conditions favorable for the setup of thermobaric instability (TI) was 2.01×10^{-7} g cm^{-3}. These conditions occurred primarily in January (47%), secon-

darily in February (36%) and March (13%), and rarely in April and December (2% each). NPTI$_{sim}$ in days decade^{-1} decreased from 43.6 in 1950–2005 to 30.5 in 2045–2099 (Table 2), a decrease of 30%; over the same time the frequency of deep mixing events decreased from 5.1 to 3.1 winters decade^{-1}, a decrease of 39% (based on the output from the CNRM-CM5 GCM, RCP8.5 scenario only, data not shown). This provided confidence that the screening for conditions potentially favorable to the setup of TI was valid.

When a weaker salinity gradient (representing our best estimate of the potential bias in simulated salinity) than the simulated gradient was used to calculate NPTI, NPTI$_{wk}$ in 1950–2005 was 47.8 days decade^{-1}, an increase of about 10% above NPTI$_{sim}$ (Table 2). The sensitivity to a weaker gradient increased slightly with time; in 2045–2099, NPTI$_{wk}$ was about 13% greater than NPTI$_{sim}$. Based on these small differences we concluded that NPTI was not highly sensitive to the magnitude of potential bias in our salinity simulations.

When a uniform salinity was used in the calculation N$_{PTI}$ increased, confirming that the 100–300 m salinity gradient makes the setup of conditions favorable to TI less common. The difference between NPTI$_u$ and NPTI$_{sim}$ can be used as a measure of how much the salinity gradient limits the setup of conditions favorable to TI through time. In 1950–2005, NPTI$_{sim}$ was 42% of NPTI$_u$ and in 2045–2099 it was 67%, indicating that the limitation imposed by the salinity gradient in setting up these conditions decreased through time, consistent with increasing N_T^2 relative to N_S^2 (ESM Fig. S2.10B).

The difference between NPTI$_{obs}$ and NPTI$_{sim}$ can be used as an indication of whether dynamically simulating the salinity gradient influences the setup of conditions favorable for TI. After 2005, NPTI$_{obs}$ is ~ 50–70% of NPTI$_{sim}$, suggesting that simulating a dynamically varying salinity results in more days favorable for TI and probably more deep ventilation events. Wood et al. (2016) used S$_{obs}$ in their simulations. The frequency of deep ventilation events reported by Wood et al. for the CNRM-CM5 GCM and RCP8.5 scenario is ~ 60% (2045–2099) of the frequency in this study for the same GCM and scenario combination. Direct comparison with Wood et al. (2016) can only be qualitative because of multiple differences in the model and methodology; nonetheless, the greater frequency of deep ventilation for this single GCM and scenario combination reported herein is consistent with the expected difference based on this analysis of NPTI$_{obs}$ and NPTI$_{sim}$.

Once TI is triggered and a deep ventilation event begins, the salinity gradient can limit the depth of deep ventilation because volumes of fresher surface water descending through increasingly saline water must stop when their density is equal to the local

Table 2

Number of days per decade that potentially favorable conditions to initiate thermobaric instability occur (NPTI). $NPTI_{sim}$: salinity profile as simulated; $NPTI_u$: salinity profile uniform at 100 mg L^{-1}, $NPTI_{wk}$: salinity profile weaker than simulated, $NPTI_{obs}$: constant salinity profile from average of measured profiles. Calculations use output from CNRM-CM5 GCM, and RCP8.5 scenario.

Period	$NPTI_{sim}$	$NPTI_u$	$NPTI_{wk}$	$NPTI_{obs}$
	days decade^{-1}			
1950–2005	43.6	103.6	47.8	48.7
2045–2099	30.5	45.8	34.5	14.7

density. The local density is a function of local temperature and salinity, so the stopping depth can be limited by the salinity gradient even if the temperature gradient would allow a deeper stopping depth. NBV_{sim} decreased from 18.2 days decade^{-1} in 1950–2005 to 2.9 days decade^{-1} in 2045–2099 (Table 3), as the 100–550 m salinity gradient, on average, got stronger through time (dominated by the gradient between 100 and 300 m, ESM Fig. S2.10B). Values of NBV were more sensitive to a weaker salinity gradient than NPTI. NBV_{wk} was greater than NBV_{sim} by 38% in 1950–2005 and by over 200% in 2045–2099 (although NBV_{wk} was still very small at $\sim$9 days decade^{-1}). This analysis indicates that the stopping depth of ventilation could be more sensitive to errors in S_{sim} than the frequency of occurrence of ventilation.

Not surprisingly, a uniform salinity increased NBV during all periods. The difference between NBV_u and NBV_{sim} is an indication of how effective the 100 to 550 m salinity gradient is at limiting deep ventilation to depths above the bottom of the lake. In 1950–2005 NBV_{sim} was 49% of NBV_u; in 2045–2099 it was 11%. This result suggests that the large-scale salinity gradient is important in determining the depth of deep ventilation, and that deep ventilation may increasingly stop at depths above the bottom in the future, as salt builds up in the LWC.

Substituting the fixed gradient S_{obs}, which reduced NPTI, instead increased NBV to 12.7 days decade^{-1} in 2045–2099, as compared to 2.9 days decade^{-1} using S_{sim}. After 1950–2005, the constant 100–500 m gradient in S_{obs} is often weaker than the dynamically simulated gradient, an effect enhanced by the redistribution of salinity to the LWC in the simulations, particularly in 2045–2099. This result suggests that using a fixed salinity gradient to model deep ventilation many decades into the future unrealistically limits the occurrence of deep mixing through its effect on decreasing N_{PTI}, but results in deeper mixing when events occur through its effect on N_{BV}.

Dissolved oxygen

The ensemble mean DO concentrations in the UWC and LWC changed very little through 2061 in both RCP scenarios (Fig. 5, ESM S2.10, Table S3.9) confirming that DO production and consumption were roughly balanced. UWC DO concentration expressed in terms of percent saturation increased starting in 2005 because water temperature was declining, but LWC percent saturation remained steady through 2050 at around 95% (ESM Fig. S2.12). In 2045–2099 the UWC ensemble mean DO concentration decreased at a rate of 0.005 and 0.031 mg L^{-1} decade^{-1}

(RCP4.5 and RCP8.5, respectively), and LWC concentrations decreased at a rate of 0.027 and 0.16 mg L^{-1} decade^{-1} (RCP4.5 and RCP8.5, respectively; Fig. 5, ESM Table S3.9). In the RCP8.5 scenario in particular, the rate of change accelerated in the years 2045–2099 (Fig. 9 and ESM S2.9), coincident with less frequent reverse stratification and deep ventilation. The greater depletion between less frequent ventilation events after 2050 can be seen in the contours of concentration from the CNRM-C5 GCM (Fig. 9).

UWC concentrations decreased but UWC percent saturation increased through 2099 (ESM Fig. S2.12), reflecting the balance between increasing temperature, which resulted in higher percent saturation values as oxygen production remained the same, and the requirement of 100% saturation at the boundary, which required removal of oxygen from the surface layer if it was super-saturated. The decreasing concentration implies more gas transfer at the surface of the lake. This could be checked with measurements if a more accurate model of DO in the UWC is desired, but for our purpose the very small decrease in concentration in the UWC ($\sim$0.1–0.2 mg L^{-1} maximum in 2099) has a small effect on the resetting of the concentration in the LWC during deep ventilation.

The ensemble means mask the high variability within a single GCM on multi-year time scales. After 2050, particularly in the RCP8.5 scenario, the difference between concentration maxima and subsequent minima increased and the time between extremes increased, within a single GCM. The local maximum and minimum values also decreased over time, which is an indication that oxygen levels were not being reset to the same baseline level that they had prior to 2050. As an example, the minimum annual LWC concentration in all of the models was 7.9 mg L^{-1} and occurred in the HadGEM2-ES model in 2088 (ESM Fig. S2.11). The previous maximum concentration in this model was 10.3 mg L^{-1} in 2071 and the next maximum was 9.2 mg L^{-1} in 2095, demonstrating the large swings in extremes and ramping down of the concentration maxima after 2050.

Discussion

Considered together, the acceleration of trends in temperature, salinity, and dissolved oxygen (Fig. 5) suggest a regime shift in the 2045–2099 timeframe for the RCP8.5 scenario. The reason for this acceleration can be traced to increases in lake surface temperature boundary condition derived from the GCM air temperature. The coldest annual lake surface temperatures, as represented by the
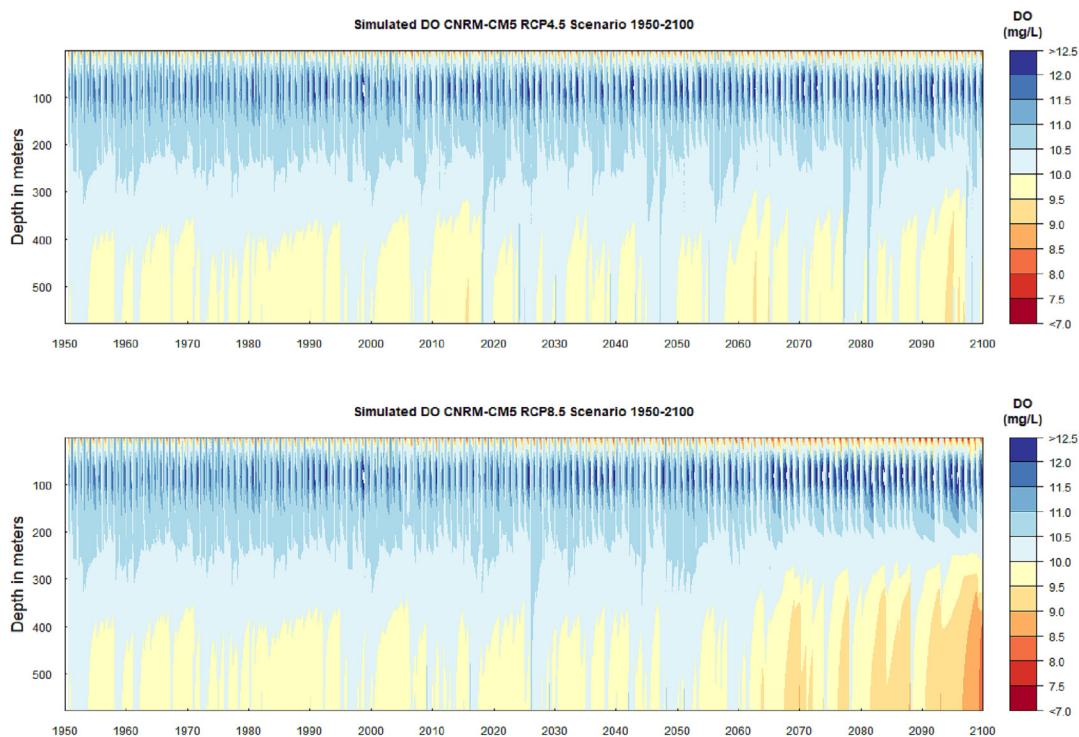
Table 3

Number of days per decade that deep ventilation could potentially occur to the bottom (NBV). NBV_{sim}: salinity profile as simulated; NBV_u: salinity profile uniform at 100 mg L^{-1}, NBV_{wk}: salinity profile weaker than simulated, NBV_{obs}: constant salinity profile from average of measured profiles. Calculations use output from CNRM-CM5 GCM, and RCP8.5 scenario.

Period	NBV_{sim}	NBV_u	NBV_{wk}	NBV_{obs}
	days decade^{-1}			
1950–2005	18.2	37.5	25.1	16.0
2045–2099	2.9	26.0	8.9	12.7

Fig. 9. Contours of dissolved oxygen concentration simulated with 1DDV model, with lake surface temperature and wind forcing provided by the CNRM-CM5 GCM, 1950–2099, 2 emissions scenarios.

10th percentile of December-May, increased more rapidly after the baseline years 1950–2005 in the RCP8.5 scenario than in the RCP4.5 scenario (Fig. 10A). In the 2045–2099 period, the winter lake surface temperatures in the RCP8.5 scenarios mostly exceed 4 °C, making wintertime reverse stratification rare. Over the same time frame, most GCMs show the highest annual wind speeds (as represented in Fig. 9 by the 90th percentile of December to May values) decreasing or remaining about the same, so the amount of energy available to initiate mixing is projected to decrease or to change little (Fig. 10B). The response to the near elimination of reverse stratification, which is necessary to initiate thermobaric mixing, is a marked decrease in the frequency of deep ventilation (Fig. 8A). The shift in the behavior of other quantities after 2050 in the RCP8.5 scenario follows: temperature in the LWC increases more rapidly (Fig. 6), salinity becomes more weighted toward the LWC (Fig. 7), and dissolved oxygen in the LWC is depleted more

rapidly (Fig. 9). Concurrent with a decrease in the frequency of deep mixing winters, there is a trend toward a larger exchange of heat (Fig. 8B), larger decrease in temperature and salinity (ESM Fig. S2.9), and a larger increase in dissolved oxygen concentration (ESM Fig. S2.11) when deep ventilation does occur. This trend toward larger adjustments with ventilation events is responsible for increasingly variable temperature, salinity, and dissolved oxygen profiles in the future.

The distinct characteristics of the RCP8.5 scenario after 2050 can also be illustrated with a simple heat balance based on the trends in heat content shown in Fig. 5 and ESM Table S3.7. If we denote the change in heat content in the LWC over a 55-year period as ΔH_{LWC} and the hydrothermal flux of heat into the LWC as G, then the difference between the two represents a flux of heat to the UWC, denoted F_{LWC}: $F_{LWC} = G - \Delta H_{LWC}$ (positive to UWC). Similarly, the flux out of the UWC to the atmosphere, F_{UWC}, is the difference
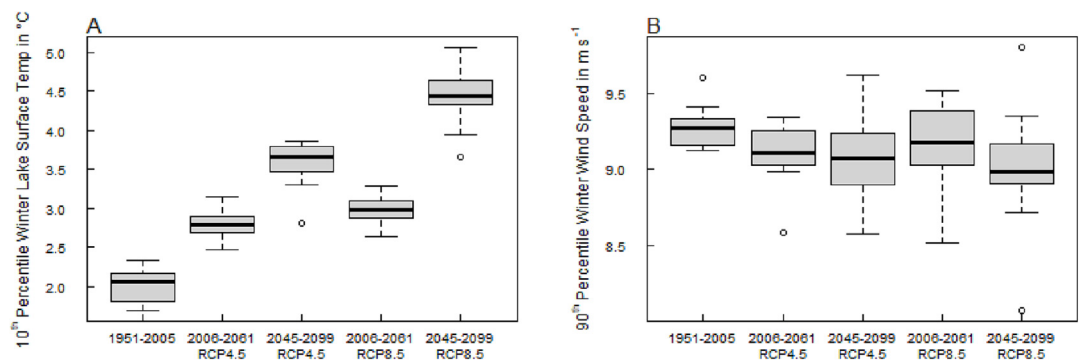

Fig. 10. A) 10th percentile of winter (December to May) lake surface temperature and B) 90th percentile of winter (December to May) wind speed used as boundary conditions in the model, over 55-year periods. The boxplots show the distribution of surface temperatures and wind speeds derived from air temperature and wind speed provided by an ensemble of 12 GCMs.

between the change in heat content in the UWC, ΔH_{UWC}, and the heat it receives from the LWC: $F_{UWC} = F_{LWC} - \Delta H_{UWC}$ (positive to atmosphere).

The historical period between 1950 and 2005 exemplifies a time when the bottom temperatures of the lake were roughly in equilibrium with the 1.4 W m^{-2} of geothermal heating to the LWC (Fig. 11, Table 4). About half of the 1.4 W m^{-2} of geothermal heating increased the temperature of the UWC and about half was eventually vented to the atmosphere. During the first 55-years of future climate simulations, more of the hydrothermal heat was used to raise temperature in the LWC, and the ensemble median of F_{LWC} decreased by 0.02 (RCP4.5) and 0.05 (RCP8.5) W m^{-2}, while the flux out of the UWC decreased by 0.15 (RCP4.5) and 0.22 (RCP8.5) W m^{-2}. Between the first and second 55-year time periods of future climate simulations, the flux from the LWC to the UWC decreased 0.03 (RCP4.5) and 0.14 (RCP8.5) W m^{-2}. In the latter half of the 21st century, particularly in the RCP8.5 scenario, there is a clear and increasing trend that more of the hydrothermal heat stays in the LWC, a consequence of reduced frequency of deep mixing that replaces water in the LWC with colder water from the UWC. In turn, more of the heat transmitted to the UWC is used to raise the temperature and is not vented to the atmosphere. In the RCP8.5 scenario, the ensemble median flux F_{UWC} in the years 2045–2099 becomes negative (-0.07 W m^{-2}, Table 4). The change in sign indicates that none of the hydrothermal heat is being vented to the atmosphere and both the geothermal inputs to the LWC and the climatic inputs from the atmosphere are heating the UWC. The result is a large increase in the projected rate of temperature increase in the 2045–2099 RCP8.5 scenario, from 0.09 to 0.18 °C decade^{-1} in the UWC, and from 0.03 to 0.11 °C decade^{-1} in the LWC. Our simulations stop at 2099, but once hydrothermal heat is no longer vented to the atmosphere, the rate of temperature change in UWC and LWC would be expected to increase and ultimately the upper limit to the rate of change in the LWC, in the complete absence of deep mixing, would be 0.39 °C decade^{-1} based on hydrothermal inputs alone.

Table 4

Ensemble median values of annual heat flux from the lower water column to the upper water column (FLWC) and from the upper water column to the atmosphere (FUWC) during 3 55-year time periods, ensemble of 12 general circulation models and 2 RCP scenarios.

		FUWC (W m^{-2})	FLWC (W m^{-2})
1950–2005	Baseline	0.65	1.39
2006–2061	RCP4.5	0.50	1.37
2045–2099	RCP4.5	0.52	1.34
2006–2061	RCP8.5	0.43	1.34
2045–2099	RCP8.5	−0.07	1.20

We can draw some conclusions about the role of salinity in inhibiting the initialization of thermobaric instabilities in Crater Lake. The initiation of thermobaric instabilities requires a small density gradient between shallow and intermediate depths, which we conceptualized to be around 100 and 300 m respectively. The gradients of both temperature and salinity must be small for the density gradient to be small. Our analysis of the results from a single GCM showed that the salinity gradient between 100 and 300 m limited the frequency of favorable thermobaric conditions to about 40% of what it would be if density were based on temperature alone (i.e., considering a homogeneous salinity profile) in the 1950–2005 period. In the period 2045–2099 (RCP8.5), the frequency of favorable thermobaric conditions was reduced compared to 1950–2005 from 43.6 to 30.5 days decade^{-1}, which corresponded to a decrease in the frequency of ventilation in this same GCM from 5.1 to 3.1 winters decade^{-1}. The increase in temperature of the UWC was the most important reason for this reduction in the frequency of favorable conditions, as the stability of the UWC measured by N^2 and the contribution of the temperature gradient to N^2 increased through time. The salinity gradient continued to be important, however. The salinity gradient limited the frequency of favorable thermobaric conditions to about 70% of what it would be if density were based on temperature alone. Thus,
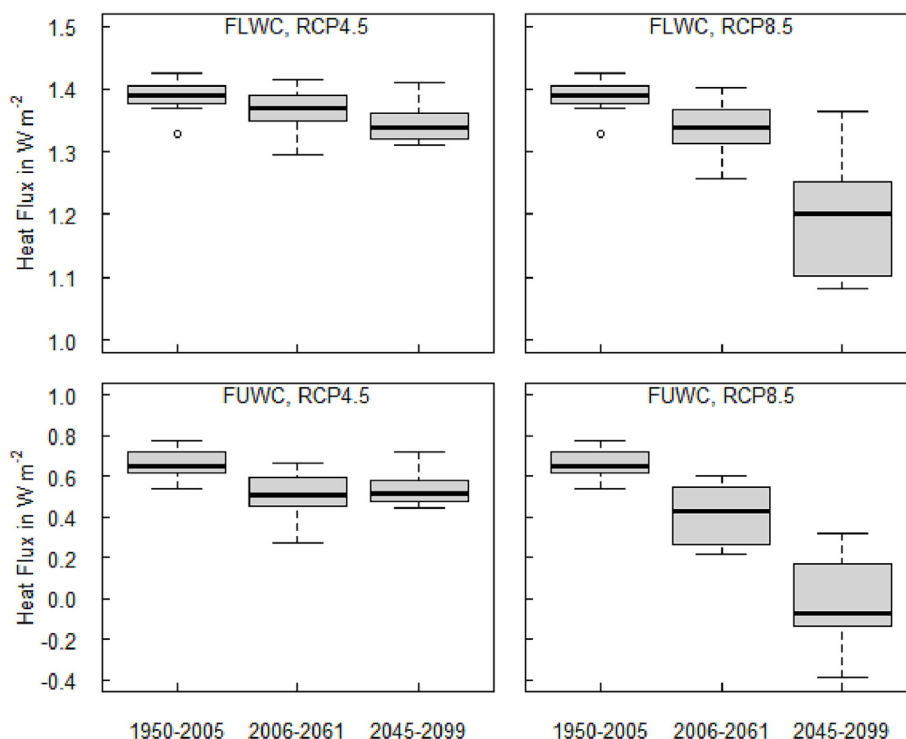

Fig. 11. Average heat flux from the lower water column (below 350 m) to the upper water column and from the upper water column to the atmosphere for three 55-year time periods, ensemble of 12 GCMs and two RCP scenarios.

the influence of salinity relative to temperature in preventing thermobaric instability is expected to be less but not insignificant in the future.

Our sensitivity analysis showed that the depth to which deep ventilation penetrates could be sensitive to long-term changes in the large-scale salinity gradient. Consequently, we suspect that the buildup of salt in the LWC resulting from a reduction in deep mixing frequency might also result in shallower depth penetration of deep mixing in the future.

Crater Lake is oligotrophic and characterized by small oxygen demands, to which the biggest contributor is the decay of organic detritus within the water column. Our increasing-with-depth volumetric rate of oxygen depletion converts to a removal of 1,516 kg of O_2 from the lake each day by the decay of organic detritus, below 350 m depth. At 10.2 mg L^{-1} the LWC (4.2×10^9 m^3) contains 4.3×10^7 kg of dissolved oxygen; therefore, the time scale required to deplete oxygen based on this rate of demand is on the order of 78 years, far longer than the time between deep ventilation events in the simulations. This low demand contrasts with Lake Tahoe, a similarly deep oligotrophic lake (Sahoo et al., 2013), and mesotrophic Lake Geneva, where the mean oxygen demand is 1.34 g O_2 m^{-2} d^{-1}, more than an order of magnitude higher than our 94 mg O_2 m^{-2} d^{-1} (Schwefel et al., 2016). At the other extreme, the expected future decay of dissolved oxygen in the deep Lake Baikal is projected to be on the order of only ±0.5 mg L^{-1} over 1,000-year simulations (Piccolroaz and Toffolon, 2018). In Norwegian fjord lakes, the dissolved oxygen profile was consistently over 90% of saturation, indicating almost no loss to decay processes (Boehrer et al., 2013). Crater Lake falls between these two extremes; over the time frame of our climate simulations the change in dissolved oxygen concentration was small, and in the most extreme scenario the minimum percent saturation in the LWC was about 75% late in the 21st century, but the rate of change was clearly accelerating toward the end of the simulations, particularly in the RCP8.5 scenario.

These simulations do not incorporate predictions about what might happen to the phytoplankton assemblage in the future under warming conditions. An ecological model would be needed to predict how changes in the vertical mixing regime affects the recycling of nutrients between the upper and lower water columns and phytoplankton growth in the photic zone, which is beyond the scope of this study. These simulations are nonetheless useful in that they isolate the effect that change in the frequency of deep ventilation would have on dissolved oxygen concentrations in the water column, while holding oxygen rate constants unchanged.

Conclusions

Our modeling has shown that climate change will alter the mixing regime and hypolimnetic temperature of Crater Lake within the 21st century. Changes will be moderate if excess radiative forcing is limited to 4.5 W m^{-2}, but the results show a clear trend in both the warming of the entire water column and a reduction in the frequency at which the very deep lake is ventilated in the future. Simulations based on the RCP8.5 scenario show the entire water column warming and importantly, reverse wintertime stratification rarely occurring in the latter half of the 21st century. An increase in the rate of change of temperature, salinity, and dissolved oxygen coincides with this near elimination of reverse stratification, so in the most extreme scenario the changes in these variables could be even larger within a few decades beyond the end of our simulations.

Crater Lake is readily compared to other very deep northern lakes that rely on thermobaric instabilities to initiate ventilation of their deepest waters. In comparison to temperate lakes of similar depth that reliably mix to the bottom every year (e.g. Bear Lake [Johnson, 1966], Quesnel Lake [Laval et al., 2012] and Great Slave Lake [Carmack and Vagle, 2021]), Crater Lake is located at a lower latitude (42.9°N), where winters are not always cold enough to produce the reverse stratification that is a necessary precursor for thermobaric instabilities to occur, and deep ventilation does not currently happen every year. This makes the deep ventilation of Crater Lake more susceptible to disruption in a warming climate than these other lakes.

Another important difference between Crater Lake and other very deep temperate lakes is that it receives consequential inputs of hydrothermal heat and salt. As a result, the temperature profile has a minimum at mid-depth, below which the salinity gradient acts to stabilize the water column. Above the temperature minimum, this stable salinity gradient further inhibits the establishment of a density gradient favorable for thermobaric instabilities. Based on the temperature gradient alone, the frequency of this condition is already low during winter and will be even lower in the future. Our analysis suggests that the salinity gradient reduces the frequency of conditions favorable for thermobaric instability by about 60% under current conditions, and that it will limit the frequency of conditions favorable for thermobaric instability by about 30% in 2045–2099 (RCP8.5), compared to the temperature gradient alone.

Even in the context of the most extreme scenario, however, hypolimnetic dissolved oxygen is expected to remain above about 75% of saturation within the 21st century. This is consistent with the oligotrophic nature of the lake and very small oxygen demands. At the current rate of oxygen demand in the lake, it would take about 70 years between deep ventilation events to remove most of the oxygen in the lake below about 350 m, the depth reached by convective mixing.

Our modeling shows the salt content in the deep lake increasing as the frequency of deep ventilation decreases. In the most severe scenario, a re-distribution of salinity from the surface to the bottom can be expected as hydrothermal fluids get trapped in the lower lake while the upper water freshens via precipitation. In addition to contributing to a reduction in the frequency of deep mixing, these shifts in the salinity profile are likely to prevent most deep ventilation events from reaching all the way to the lake bottom due to increasing water density with depth.

Historically, the hydrothermal heat added to the lake within the crater has been vented to the atmosphere. This transfer of heat between the lower and upper water columns during mixing events and subsequent transfer of heat to the atmosphere has prevented the buildup of heat and rising temperature in the lake even in the presence of hydrothermal heating. If excess radiative forcing is not limited to 4.5 W m^{-2}, our simulations show that by the end of the 21st century the hydrothermal heat will cease to be vented to the atmosphere and the atmosphere, instead of cooling the lake, will warm it from above. If this occurs, the temperature of the deep waters of the lake can be expected to increase rapidly. The upper limit for the rate of increase in the hypolimnion is 0.39 °C decade^{-1} from hydrothermal heating alone.

This study shows that the subset of very deep lakes that receive hydrothermal fluids that carry heat and salt can be particularly susceptible to alterations in their mixing regime, depending on their latitude and altitude. Such lakes will not be easily categorized without studies of their idiosyncratic features. The heat and salt fluxes are unique to each lake, and the magnitude and ratio of these will determine how easily the mixing regime can be altered and how resistant the hypolimnion will be to climate warming.

CRediT authorship contribution statement

Tamara Wood: Conceptualization, Funding acquisition, Formal analysis, Writing – original draft, Supervision, Project administration. **Susan Wherry:** Software, Formal analysis, Investigation, Visualization, Writing – review & editing. **Sebastiano Piccolroaz:** Methodology, Software, Writing – review & editing. **Scott Girdner:** Conceptualization, Funding acquisition, Data curation, Investigation, Writing – review & editing.

Declaration of Competing Interest

The authors declare that they have no known competing financial interests or personal relationships that could have appeared to influence the work reported in this paper.

Acknowledgements

Appendix A. Supplementary data

Supplementary data to this article can be found online at https://doi.org/10.1016/j.jglr.2023.03.014.

References

Abatzoglou, J.T., Brown, T.J., 2012. A comparison of statistical downscaling methods suited for wildfire applications. Int. J. Climatol. 32, 772–780.

Boehrer, B., Fukuyama, R., Chikita, K., 2008. Stratification of very deep, thermally stratified lakes. Geophys. Res. Lett. 35.

Boehrer, B., Golmen, L., Løvik, J.E., Rahn, K., Klaveness, D., 2013. Thermobaric stratification in very deep Norwegian freshwater lakes. J. Great Lakes Res. 39, 690–695.

Bowie, G.L., Mills, W.B., Porcella, D.B., Campbell, C.L., Pagenkopf, J.R., Rupp, G.L., Johnson, K.M., Chan, P., Gherini, S.A., Chamberlin, C., 1985. Rates, Constants, and Kinetics Formulations in Surface Water Quality Modeling. Environmental Protection Agency, Washington, D.C.

Carmack, E., Vagle, S., 2021. Thermobaric processes both drive and constrain seasonal ventilation in Deep Great Slave Lake, Canada. J. Geophys. Res.: Earth Surface 126. e2021JF006288.

Carmack, E.C., Weiss, R.F., 1991. Convection in lake Baikal: an example of thermobaric instability. In: Chu, P.C., Gascard, J.C. (Eds.), Deep Convection and Deep Water Formation in the Oceans. Elsevier, Amsterdam, pp. 215–228.

Chen, C.-T.-A., Millero, F.J., 1986. thermodynamic properties for natural waters covering only the limnological range1. Limnol. Oceanogr. 31, 657–662.

Collier, R., Dymond, J., McManus, J., 1990. Chemical and physical properties of the water column at Crater Lake, Oregon. In: Drake, E.T., Larson, G.L., Dymond, J., Collier, R. (Eds.), Sixty-ninth Annual Meeting of the Pacific Division/American Association for the Advancement of Science. Pacific Division of the American Association for the Advancement of Science. Oregon State University, Corvallis, Oregon, p. 221.

Crawford, G., Collier, R., 2007. Long-term observations of deepwater renewal in Crater Lake, Oregon. Hydrobiologia 574, 47–68.

Diaz-Nieto, J., Wilby, R.L., 2005. A comparison of statistical downscaling and climate change factor methods: impacts on low flows in the River Thames, United Kingdom. Clim. Change 69, 245–268.

Dymond, J., Collier, R.W., McManus, J., Larson, G.L., 1996. Unbalanced particle flux budgets in Crater Lake, Oregon: Implications for edge effects and sediment focusing in lakes. Limnol. Oceanogr. 41, 732–743.

Eklund, H., 1965. Stability of lakes near the temperature of maximum density. Science 149, 632–633.

Fennel, K., Collier, R., Larson, G., Crawford, G., Boss, E., 2007. Seasonal nutrient and plankton dynamics in a physical-biological model of Crater Lake. In: Larson, G. L., Collier, R., Buktenica, M.W. (Eds.), Long-term Limnological Research and Monitoring at Crater Lake, Oregon: A Benchmark Study of a Deep and Exceptionally Clear Montane Caldera Lake. Springer, Netherlands, Dordrecht, pp. 265–280.

Forsythe, W.C., Rykiel, E.J., Stahl, R.S., Wu, H.-I., Schoolfield, R.M., 1995. A model comparison for daylength as a function of latitude and day of year. Ecol. Model. 80, 87–95.

Gu, H., Jin, J., Wu, Y., Ek, M., Subin, Z., 2013. Calibration and validation of lake surface temperature simulations with the coupled WRF-lake model. Clim. Change 129.

Henderson-Sellers, B., 1985. New formulation of eddy diffusion thermocline models. App. Math. Model. 9 (4), 441–446. https://doi.org/10.1016/0307-904X (85)90110-6.

Hijmans, R.J., 2019. meteor: Meteorological Data Manipulation. R package version 0.3-4.

Imerito, A., 2014. Dynamic Reservoir Simulation Model DYRESM v4–v4.0 Science Manual. University of Western Australia, Centre for Water Research, Perth.

Jassby, A., Powell, T., 1975. Vertical patterns of eddy diffusion during stratification in Castle Lake, California. Limnol. Oceanogr. 20, 530–543.

Johnson, L., 1966. Temperature of maximum density of fresh water and its effect on circulation in Great Bear Lake. J. Fish. Res. Board Can. 23, 963–973.

Laval, B.E., Vagle, S., Potts, D., Morrison, J., Sentlinger, G., James, C., McLaughlin, F., Carmack, E.C., 2012. The joint effects of riverine, thermal, and wind forcing on a temperate fjord lake: Quesnel Lake, Canada. J. Great Lakes Res. 38, 540–549.

McIntire, C.D., Larson, G.L., Truitt, R.E., 2007. Seasonal and interannual variability in the taxonomic composition and production of phytoplankton assemblages in Crater Lake, Oregon. Hydrobiologia 574, 179–204.

McManus, J., Collier, R.W., Chen, C.-T.-A., Dymond, J., 1992. Physical properties of Crater Lake, Oregon: a method for the determination of a conductivity- and temperature-dependent expression for salinity. Limnol. Oceanogr. 37, 41–53.

McManus, J., Collier, R.W., Dymond, J., 1993. Mixing processes in Crater Lake, Oregon. J. Geophys. Res. 98, 18295–18307.

McManus, J., Collier, R.W., Dymond, J., Wheat, C.G., Larson, G.L., 1996. Spatial and temporal distribution of dissolved oxygen in Crater Lake, Oregon. Limnol. Oceanogr. 41, 722–731.

Minville, M., Brissette, F., Leconte, R., 2008. Uncertainty of the impact of climate change on the hydrology of a nordic watershed. J. Hydrol. 358, 70–83.

Munk, W.H., Anderson, E.R., 1948. Notes on a theory of the thermocline. J. Mar. Res. 7, 276–295.

Nathenson, M., 1990. Crater Lake climate and lake level variability. In: Drake, E.T., Larson, G.L., Dymond, J., Collier, R. (Eds.), Sixty-ninth Annual Meeting of the Pacific Division/American Association for the Advancement of Science. Pacific Division of the American Association for the Advancement of Science. Oregon State University, Corvallis, Oregon, p. 221.

Neal, V.T., Neshyba, S.J., Denner, W.W., 1972. Vertical Temperature Structure in Crater Lake, Oregon. Limnol. Oceanogr. 17, 451–454.

Pacanowski, R.C., Philander, S.G.H., 1981. Parameterization of Vertical Mixing in Numerical Models of Tropical Oceans. J. Phys. Oceanogr. 11, 1443–1451.

Panofsky, H.A., Brier, G.W., 1968. Some applications of statistics to meteorology. Earth and Mineral Sciences Continuing Education, College of Earth and Mineral Sciences, University Park, Pa.

Perroud, M., Goyette, S., Martynov, A., Beniston, M., Annevillec, O., 2009. Simulation of multiannual thermal profiles in deep Lake Geneva: A comparison of one-dimensional lake models. Limnol. Oceanogr. 54, 1574–1594.

Piccolroaz, S., 2016. Prediction of lake surface temperature using the air2water model: guidelines, challenges, and future perspectives. Adv. Oceanogr. Limnol. 7.

Piccolroaz, S., Healey, N.C., Lenters, J.D., Schladow, S.G., Hook, S.J., Sahoo, G.B., Toffolon, M., 2018. On the predictability of lake surface temperature using air temperature in a changing climate: a case study for Lake Tahoe (U.S.A.). Limnol. Oceanogr. 63, 243–261.

Piccolroaz, S., Toffolon, M., 2013. Deep water renewal in Lake Baikal: a model for long-term analyses. J. Geophys. Res. 118, 6717–6733.

Piccolroaz, S., Toffolon, M., 2018. The fate of Lake Baikal: how climate change may alter deep ventilation in the largest lake on Earth. Clim. Change 150, 181–194.

Piccolroaz, S., Toffolon, M., Majone, B., 2013. A simple lumped model to convert air temperature into surface water temperature in lakes. Hydrol. Earth Syst. Sci. 17, 3323–3338.

Piccolroaz, S., Zhu, S., Ptak, M., Sojka, M., Du, X., 2021. Warming of lowland Polish lakes under future climate change scenarios and consequences for ice cover and mixing dynamics. J. Hydrol.: Reg. Stud. 34, 100780.

Powell, T., Jassby, A., 1974. The estimation of vertical eddy diffusivities below the thermocline in lakes. Water Resour. Res. 10, 191–198.

Redmond, K.T., 1990. Crater Lake climate and lake level variability. In: Drake, E.T., Larson, G.L., Dymond, J., Collier, R. (Eds.), Sixty-ninth Annual Meeting of the Pacific Division/American Association for the Advancement of Science. Pacific Division of the American Association for the Advancement of Science. Oregon State University, Corvallis, Oregon, p. 221.

Redmond, K.T., 2007. Evaporation and the hydrologic budget of Crater Lake, Oregon. Hydrobiologia 574, 29–46.

Riahi, K., Rao, S., Krey, V., Cho, C., Chirkov, V., Fischer, G., Kindermann, G., Nakicenovic, N., Rafaj, P., 2011. RCP 8.5—a scenario of comparatively high greenhouse gas emissions. Clim. Change 109, 33–57.

Rupp, D.E., Abatzoglou, J.T., Hegewisch, K.C., Mote, P.W., 2013. Evaluation of CMIP5 20th century climate simulations for the Pacific Northwest USA. J. Geophys. Res. Atmos. 118, 10884–10906. https://doi.org/10.1002/jgrd.50843.

Sahoo, G.B., Schladow, S.G., Reuter, J.E., Coats, R., Dettinger, M., Riverson, J., Wolfe, B., Costa-Cabral, M., 2013. The response of Lake Tahoe to climate change. Clim. Change 116, 71–95.

Schwefel, R., Gaudard, A., Wüest, A., Bouffard, D., 2016. Effects of climate change on deepwater oxygen and winter mixing in a deep lake (Lake Geneva): comparing observational findings and modeling. Water Resour. Res. 52, 8811–8826.

Subin, Z.M., Riley, W.J., Mironov, D., 2012. An improved lake model for climate simulations: Model structure, evaluation, and sensitivity analyses in CESM1. J. Adv. Model. Earth Syst. 4.

Sweers, H.E., 1970. Vertical diffusivity coefficient in a thermocline. Limnol. Oceanogr. 15, 273–280.

Taylor, K., Ronald, S., Meehl, G., 2012. An overview of CMIP5 and the experiment design. Bull. Am. Meteorol. Soc. 93, 485–498.

Thomson, A., Calvin, K., Smith, S., Kyle, P., Volke, A., Patel, P., Delgado Arias, S., Bond-Lamberty, B., Wise, M., Clarke, L., Edmonds, J., 2011. RCP4.5: A pathway for stabilization of radiative forcing by 2100. Clim. Change 109, 77–94.

Urbach, E., Vergin, K.L., Young, L., Morse, A., Larson, G.L., Giovannoni, S.J., 2001. Unusual bacterioplankton community structure in ultra-oligotrophic Crater Lake. Limnol. Oceanogr. 46, 557–572.

van Haren, H., Piccolroaz, S., Amadori, M., Toffolon, M., Dijkstra, H.A., 2020. Moored observations of turbulent mixing events in deep Lake Garda, Italy. J. Limnol. 80 (1). https://doi.org/10.4081/jlimnol.2020.1983.

Weiss, R.F., 1992. Rates and variability of deep water renewal and biological production in deep temperate lakes: Lake Baikal and Crater Lake (abstract). Eos Transactions AGU, Fall Meeting Supplemental 73, 198.

Wherry, S.A., Piccolroaz, S., Wood, T.M., Girdner, S.F., 2023, in progress. 1-D Deep Ventilation (1DDV) model for Crater Lake, Oregon, 1950-2100. U. S. Geological Survey data release, doi: 10.5066/P5096NLDLX.

Wood, T.M., Wherry, S.A., Piccolroaz, S., Girdner, S.F., 2016. Simulation of deep ventilation in Crater Lake, Oregon, 1951–2099, Scientific Investigations Report, Reston, VA.

Xiao, C., Lofgren, B.M., Wang, J., Chu, P.Y., 2016. Improving the lake scheme within a coupled WRF-lake model in the Laurentian Great Lakes. J. Adv. Model. Earth Syst. 8, 1969–1985.